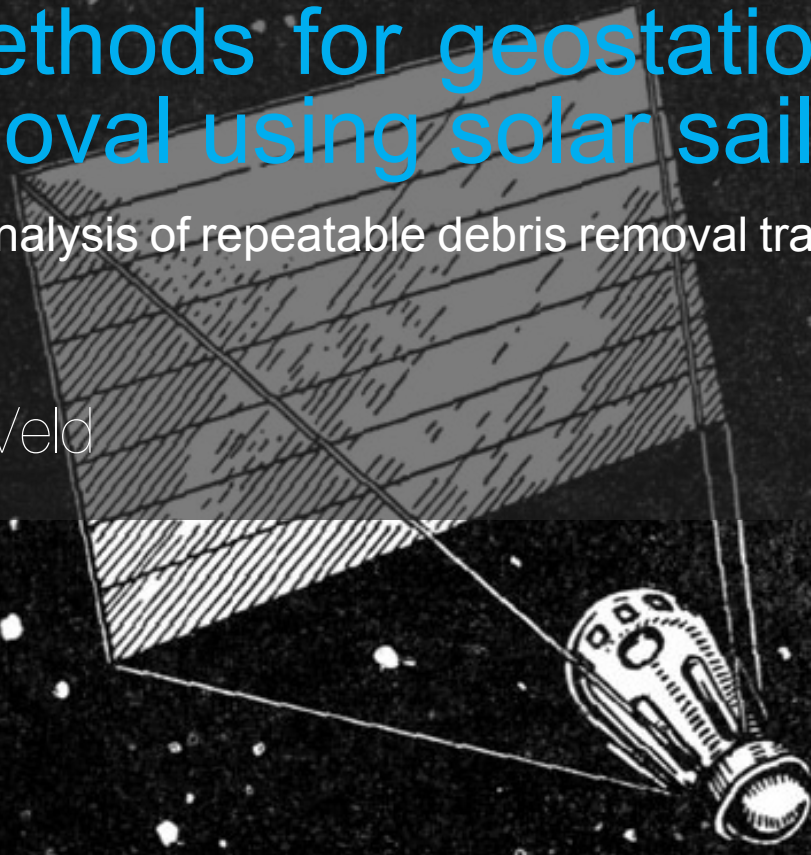# Control methods for geostationary debris removal using solar sailing

A hybrid low-thrust analysis of repeatable debris removal trajectories

MSc Thesis

Frank Timon de Veld

Delft University of Technology

TUDelft

Control methods for geostationary debris removal using solar sailing

A hybrid low-thrust analysis of repeatable debris removal trajectories

by

Frank Timon de Veld

Frank de Veld   5126576

Main supervisor:	Dr. Jeannette Heiligers
External supervisor:	Dr. Hanspeter Schaub
Chair of committee:	Dr. Wouter van der Wal
Examiner	Dr. Stefano Speretta
Assistant supervisor:	Ir. Livio Carzana
Project Duration:	June, 2021 - November, 2022
Faculty:	Faculty of Aerospace Engineering, Delft

Cover: Solar Sailing, illustration from a 1967 Soviet book 'The milestones of the Space Epoch' by M. Vasiliev. Artist unknown.

TUDelft

Nothing in my way
Keane

Acknowledgements

I am writing this, officially just in the fourth year of my Master's. This all took a bit longer than I had in mind, but then many things did not happen exactly as planned in the past few years. And for most of them, I am happy that they went that way. I truly am sad this study will come to an end for me now. I only switched to space a few years ago, when I started this Master's, knowing it would have been more straightforward to continue with physics or mathematics which I had studied before. But I chose space, and I think this decision was an impactful one and probably the best one I have made in my life.

I mostly want to thank Jeannette Heiligers, my main supervisor, and Livio Carzana, in practice my co-supervisor. They have helped me tremendously by listening to my thoughts every week, helping me through tough times, and having no problem at all with the fact that I spent so much time on other activities during the thesis. The weekly meetings, despite interruptions from these activities, provided me with much-needed structure during my working days.

Many thanks as well to dr. Schaub from the University of Colorado Boulder, who assisted me with my goal of coming to Boulder as a visiting scholar from the very start in March 2020. While two and a half years of continuous attempts of arranging this stay did not reach the end I was hoping for, I also do not regret all this effort at all, and I am very thankful for the support received throughout my thesis from almost 8000 km away.

While the conclusion of this thesis was not what I had hoped and expected beforehand, I am nevertheless proud. That is also science, it also adds to the knowledge of the subject, and that should not be forgotten. Without this realisation, one cannot be a good researcher.

Of course, thanks to my friends and family for being by my side and listening to me talking, and complaining, about my thesis progress. Without you this would have been much less enjoyable. A special thanks for my friends from Ecosmic, with whom I have started an amazing project, demanding much of my thesis time, but I would not have it any other way. I wish you the best of luck!

My interest for the solar sailing has also increased tremendously since I started to work on this topic, first during the literature study and then during the real work, the thesis. At first it was merely an interesting topic for me, but now I am truly amazed with what has been made possible in the field of solar sailing, and the tremendous potential this concept have. I believe solar sailing can become a core part of space flight and I hope research and funding in the coming years will be able to apply this potential in space missions.

What I truly found special was the look of amazement on so many faces when I talked about my thesis, especially with people outside of the 'space world'. It is sometimes easy to forget in what kind of amazing sector we work and study in, and conversations like these often made me reflect and 're-find' enthusiasm about this subject which I am so passionate about.

Frank de Veld
Delft, November 2022

Summary

Solar sailing is a spacecraft propulsion method distinguished by the fact that no propellant is used, but instead acceleration is the consequence of solar radiation pressure (SRP) on large, thin sails whose orientation can be changed to control the acceleration magnitude and direction of the sailcraft. However, contrary to conventional propulsion systems, the acceleration magnitude and direction are strongly correlated for solar sailing, which makes solar-sail control a unique branch of satellite control theory. The characteristics of solar sailing lend themselves well for space missions requiring long, continuous accelerations, a large ΔV and large flight times in the order of years or decades. Examples include solar polar orbiters and interstellar flights, mission applications which are very difficult or impossible with conventional propulsion systems.

This thesis work explores a different mission application, namely repeatable space debris removal, specifically in the geostationary belt. Space debris is becoming a significant threat to satellites and more and more costly collision avoidance manoeuvres are required to keep satellites safe. While this threat is mostly present in low-Earth orbits, geostationary orbits and other high-altitude orbits see other dangers, such as the fact that debris in these regions do not de-orbit naturally. To keep these environments safe for the present and future, dangerous debris objects must be removed by an external satellite. This however is expensive, mostly because active debris removal mission concepts only envision one removed debris object per mission due to fuel constraints. This thesis work demonstrates how solar sailing could be employed as a main method of propulsion instead, with a focus on minimising the total mission time of re-orbiting a debris object to a safe region and returning without the debris object to geostationary orbit. For this goal, analytical control methods for the sail are used, contrary to numerical control optimisation methods found in literature. The many-revolution trajectories combined with the strong correlation between solar-sail acceleration magnitude and direction make numerical optimisation of the trajectory in terms of mission time a lengthy procedure compared to the relatively simple approach of analytical control methods. The applicability of these control methods to this specific test case is analysed in this work. Additionally, the possibility of adding a solar-electric-propulsion (SEP) acceleration is analysed, for which the acceleration magnitude and direction are not correlated.

The geostationary belt is a region protected through guidelines of the Inter-Agency Space Debris Coordination Committee, defined through an altitude interval between 35,586 km and 35,986 km and a latitude interval between -15° and 15°. At their end-of-life, geostationary satellites move themselves to a graveyard orbit above the geostationary belt with the remaining fuel they have, whenever possible. The altitude difference is at minimum 235 km and determined through the area-to-mass ratio of the object. While this value is often unknown for debris objects such as solar panel pieces or fuel tanks, a relation between the area and the mass can be employed instead. In this work, a sailcraft for debris removal with a mass of 500 kg is used, debris masses are varied between 250 kg and 1000 kg, sail sizes are varied between 7500 m^2 and 15000 m^2 and SEP-thrust levels between 0.5 and 2.5 mN are used.

A perfectly reflecting solar-sail model and a simple discontinuous eclipse model are used. Modified equinoctial orbital elements are used, along with a Runge-Kutta 4 (RK4) integrator. In the dynamical model the five accelerations with the largest magnitude at geostationary altitude (41267 km) are considered, namely the point-mass gravity acceleration of the Earth, Moon and Sun, the SRP acceleration and the acceleration due to the J_2-zonal harmonic, along with the SEP acceleration when used.

Regarding the control methods, the accessibility-and-deficit (A^nD) blending method is primarily analysed. This is a method which combines several locally optimal steering laws based on the resulting thrust magnitude (accessibility) and how much time it would take to achieve the target orbital element with this thrust direction (deficit). The locally optimal steering laws themselves are the result of analytical optimisation using Lagrange's variational equations.

The results of this control algorithm are validated using literature results. Subsequently, a sensitivity analysis is performed on the results from the A^nD blending algorithm, in which the debris mass, sail area and propagation starting time are varied. Comparison with three literature validation test cases and their results in terms of mission time shows that analytical control methods such as the A^nD blending method do not result in trajectories with mission times comparable to the ones obtained through numerical optimisation. Using initial conditions from literature, the trajectories obtained by means of analytical control strategies showed round-trip mission times ranging from 630 days to 760 days, which is in the order of 1.4 to 5.1 times larger than mission times from literature. One reason for this result is the inability of the A^nD blending method to bound both the semi-major axis and the eccentricity during the mission segment to the graveyard orbit. Subsequently, it takes a long time to decrease these values again to match the orbital elements of the geostationary region. Additionally, it has been found that the locally optimal steering laws on which the A^nD blending method is based show a large seasonal variation in the resulting

cone angles and therefore a large variation in mission times for different mission start dates. This result was not found to such an extent for numerical control methods from literature.

The sensitivity of the mission time results from the A^nD blending method for a variation of parameters like the mission start date, sail area and debris mass has been studied. With these results, analytical control methods, such as the A^nD blending method, could be applied for preliminary analysis of mission time results for a range of relevant parameters. Possibly, optimised mission times from numerical control could be predicted before propagation if the factor difference between the analytical and numerical results is known, but more research is needed in this area. For the mission start date, the shortest mission times are found for starting dates just after the solstices, while starting dates just after the equinoxes lead to the longest mission times. A relationship between the sail size and the time of flight is found which resembles an exponential relationship. A lack of dependence between the debris mass and the time of flight is found, which is a consequence of the control of the A^nD blending method and should not be seen as a result which can be generalised.

The usage of an SEP acceleration has been found to be very influential on the results, halving the mission time for an SEP acceleration of 1% of the maximum SRP acceleration. This result follows from the large cone angles following the A^nD blending control, though relatively large cone angles are seen in literature too.

It is recommended to perform further analysis on the relation between mission time results obtained through analytical control with those obtained through numerical control. What is mostly lacking in the state-of-the-art is a catalogue of realistic mission parameters and the associated optimised mission times obtained through numerical control methods, as an optimised mission time is currently only known for one set of realistic mission parameters. To increase the realism of this mission concept, it is recommended to also investigate solar-sail-assisted rendezvous and debris capture dynamics further.

Contents

Nomenclature

Abbreviations

Abbreviation	Definition
A^{n}D	Accessibility-and-deficit
ECI	Earth-centered inertial
ECEF	Earth-centered, Earth-fixed
ESA	European Space Agency
GEO	Geostationary orbit
ITU	International Telecommunications Union
JAXA	Japanese Aerospace Exploration Agency
LEO	Low Earth orbit
MEOE	Modified equinoctial orbital elements
NASA	National Aeronautics and Space Administration
NEA	Near-Earth asteroid
PMG	Point-mass gravity
RK4	Runge-Kutta 4
SEP	Solar electric propulsion
SRP	Solar radiation pressure
TBD	Third-body dynamics

Symbols

Symbol	Definition	Unit
a	Semi-major axis	[km]
$\vec{a}$	Acceleration vector	[-]
e	Eccentricity	[-]
r_p	Radius of Pericenter	[km]
t_0	Initial epoch	[JD]
W_k	Weight factor for the orbital element k	[-]
α	Solar sail cone angle	[deg]
δ	Solar sail clock angle	[deg]
$\hat{\lambda}$	Ideal thrust direction	[-]
ν	True anomaly	[deg]
Ω	Longitude of the ascending node	[deg]
ω	Argument of periapsis	[deg]
$\mathcal{E}_{ECI}$	ECI reference frame	
$\mathcal{E}_{ECEF}$	ECEF reference frame	

List of Figures

List of Tables

1

Introduction

Traditionally, spacecraft have been very dependent on propellant consumption to move in a desired direction, just like most vehicles need fuel to move forward. However, this is not the case for all vehicles. The energy required for movement can come from fuel or other internally stored sources of energy, but there is also an abundance of energy in the outside world. A clear example of this is sailing, where the wind is used to travel large distances over sea or land without consuming any fuel. This method of propulsion has been used since prehistoric times [1]. Seemingly, this analogy does not fully transfer to the vacuum of space, without any air to allow wind flows or any water to sail through.

This changed with the discoveries on electromagnetism by Maxwell in the 1860s, which showed that light itself carries momentum and transfers it to objects upon collision [2]. It did not take long to realise the potential for space flight, and the French writer Jules Verne is commonly attributed with the first recognition that light could be used to manoeuvre spacecraft - almost 100 years before the first satellite was launched [3]. However, the very small pressure ($4.56 \cdot 10^{-6}$ N m^{-2} [4] at 1 AU) of solar radiation pressure made this idea of 'solar sailing' still very futuristic. With the discoveries by Konstantin Tsiolkovsky and Friedrich Tsander in the 1920s, the first technical papers about solar sailing were written, as the spacecraft concepts introduced required "tremendous mirrors of very thin sheets" [5]. However, it took until the 1970s for solar sailing to be seen as a realistic option by a space agency, namely the National Aeronautics and Space Administration (NASA). A rendezvous mission with Halley's comet was planned and a wide variety of options were discussed for initial selection. The solar-sail option, requiring an area of 0.6 km^2, was not selected and neither did the mission itself launch, but for the first time the concept of solar sailing was the subject of practical research [4].

Only in 2010, the first solar-sail mission, named IKAROS, was launched by the Japanese Aerospace Exploration Agency (JAXA). This was an interplanetary mission for technology demonstration. The following decade, organisations like NASA, the Planetary Society and several universities have flown small solar sails with sail areas up to a few tens of square meters. All of them were technology demonstration missions, used to understand the principles of solar sailing in orbit or to test the deployment mechanisms. Since the structure of a solar sail is relatively simple, the development costs are very low compared to other space missions, allowing smaller organisations to work on solar-sail development as well [4]. The Near-Earth Asteroid (NEA) Scout mission scheduled for launch in November 2022 is expected to be the first mission where solar sailing is used to enable scientific mission goals, namely the reconnaissance with a NEA [6].

However, the potential of solar sailing is much larger than this application alone. Theoretical research has shown many novel applications for solar sailing and some of these are virtually impossible without the usage of solar sails, such as solar storm warning missions [7], solar polar orbit missions [8] and interstellar travel [9]. One of the advantages of solar sailing lies in the acceleration. While the acceleration due to solar radiation pressure is very small even for large sails, the crucial difference with conventional methods of spacecraft propulsion is that solar sails provide a continuous acceleration during the entire mission. Combined with the second advantage that no propellant is needed, very long-lasting solar-sail missions are possible with large changes in the orbital energy. While practical research on the engineering of solar sails does not enable most of these mission proposals yet, many of these could be possible in the near future. One such example is the usage of solar sailing for space debris removal.

Since the launch of the first satellite Sputnik I in 1959, objects have accumulated in Earth-centered orbits. Collectively, these objects are known as 'space debris', making a distinction with natural (micro)-asteroids. Space debris cover objects such as defunct satellites, rocket stages and boosters, solar panels, paint flakes and any other object which intentionally or unintentionally has been left in orbit. Approximately 30,000 debris objects are currently tracked from Earth, but statistical models from the European Space Agency (ESA) estimate the presence of 34,000 debris objects greater than 10 cm in orbit around Earth, 900,000 debris objects in between 1 cm and

10 cm in size and 128 million objects in between 1 mm to 1 cm [10]. The danger associated to these space-debris pieces is that they can collide with active satellites or other debris objects with relative speeds in the order of 10 km/s, thus creating even more space debris. At worst, there is a fear for the so-called Kessler syndrome, where collisions will create a cascading effect resulting in a dense cloud of space debris around Earth, paralysing current and future spaceflight activities [11]. Even when this would not occur, a growing number of space debris objects results in much work for tracking these objects and preparing satellites to perform manoeuvres to avoid collisions. This is especially problematic for regions in space which are dense in satellites, like the geostationary belt.

The geostationary belt has the unique property that the ground track of any object in this belt appears stationary from an observer on Earth, as the object orbits exactly at the same rate as Earth's rotation rate. Orbits in this belt are of particular interest for telecommunication satellites and this orbital region is actively managed by the International Telecommunications Union (ITU), which allocates orbital slots here. While this is mostly needed to avoid communication interference rather than to avoid collisions, there are many uncontrolled and dangerous objects nearby active satellites which pose a significant risk [12]. Unlike objects in Low Earth Orbit (LEO), objects in Geostationary Orbit (GEO) do not naturally de-orbit due to the absence of atmospheric drag. For active satellites, international guidelines set up by the Inter-Agency Debris coordination committee (IADC) mention that any satellite must be removed from this geostationary belt within 25 years of its mission end. This usually results in an orbit-raising manoeuvre of approximately 240 km using propellant left over for this purpose specifically. However, for older satellites and individual debris pieces, active debris removal by an external satellite is needed, and additionally not all active satellites succeed in this orbit-raising manoeuvre at their end-of-life. One of the first such active debris removal missions is ClearSpace-1, scheduled to launch in 2025 [13].

To achieve such an active debris removal mission using solar sailing as the method of propulsion, solar-sail control algorithms are needed to determine the optimal acceleration magnitude and direction throughout the trajectory. The usage of solar sails introduces some complications, as thrust in the direction of incoming sunlight is impossible to achieve and the acceleration magnitude is strongly related to the acceleration direction. The trajectories needed for GEO debris removal are also planet-centred and involve very small accelerations, leading to tens or hundreds of revolutions before a successful re-orbit. This can complicate the control of solar sails and optimisation of the trajectory in terms of mission time. For relatively simple mission goals, such as targeting one specific orbital element, an optimal acceleration direction can be found analytically based on dynamical model assumptions. Methods based on such assumptions are known as locally optimal steering laws and are applicable to target any orbital element, or parameters based on these elements [14]. When instead two or more orbital elements are targeted, these optimal acceleration directions can be combined using weight functions. Examples include pericenter-semi-major axis blending [15] and blending based on accessibility and deficit scores with the A^nD blending method of Macdonald and McInnes [16]. These analytical methods rely on finding an optimal acceleration direction based on certain assumptions, though numerical optimisation methods including the constraints necessary for solar sailing have also been used extensively in literature, for example for planet-centred solar sailing includes usage of differential dynamic programming (DDP) techniques [17].

To make the concept of solar sailing for GEO debris removal even more feasible, a low-thrust propulsion system like solar electric propulsion (SEP) can be added. These propulsion systems are commonly used in geostationary satellites for station-keeping manoeuvres and end-of-life management. They are very propellant-efficient, though can only provide very small thrust levels. Since SEP has an extensive flight heritage, it is conceivable that a first prototype for a debris removal mission would also make use of such a method of propulsion to bridge the gap between theory and application in the field of solar sailing. The concept of SEP-assisted solar-sail missions has been researched previously [18], [19].

Determining the control law of this SEP engine can also be done numerically. However, this increases the number of degrees of freedom from two (two solar-sail attitude angles) to five (two solar-sail attitude angles, two SEP-thrust angles and an SEP-thrust magnitude), therefore drastically increasing the problem complexity. On the other hand, this concept of adding SEP propulsion can be analysed analytically and implemented in existing control blending methods. This makes the A^nD blending method of Macdonald and McInnes especially interesting to be considered, since the SEP acceleration can be implemented analytically in the control.

1.1. Research objective

To this day, the concept of active GEO debris removal using solar sailing has been studied to a limited extent in literature, especially considering its potential for repeatable debris removal. With only one sailcraft, potentially tens of debris objects can be removed in a single mission. This work aims to present a complete overview of mission times for one removal cycle for various parameters such as debris mass, solar-sail area and mission starting date, obtained through analytical control methods instead of numerical control methods. Through this analysis, the potential of solar-sailing for repeatable GEO debris removal is mapped. Additionally, the added value of an SEP engine for this type of mission case is studied. The feasibility of the A^nD blending method compared to numerical control techniques as the analytical solar-sail and SEP-control method is primarily studied in this work.

1.2. Research questions

As discussed in Section 1.1, the focus of this work is on mapping the potential of solar-sailing/SEP-hybrid spacecraft for repeated GEO space debris removal. This is done using the A^nD blending method as a control algorithm to assess its feasibility for this use case. To achieve this research objective, the following research questions must be answered:

- 1. Do analytical control methods for solar sailing form a usable alternative to numerical control methods for trajectory planning for one cycle from GEO to the graveyard orbit and back?
- 2. What is the minimal time required for re-orbiting geosynchronous debris to the graveyard orbit and manoeuvring back to GEO using solar sailing as the only form of propulsion?

    (a) How do parameters like mission start date, solar-sail area, debris mass and debris orbital parameters influence the mission time results?

    (b) How does additional usage of an SEP engine influence mission time results?
- 3. Is it possible to explain the influence of SEP thrust on the minimal-time results analytically?
- 4. Does solar sailing form an advantageous form of propulsion for GEO debris removal compared to existing propulsion methods?

1.3. Report Outline

The main part of this thesis is written in the form of a journal article manuscript in Chapter 2, formally defining the main case study and the control algorithms used as well as presenting an analysis of the results. Chapter 3 discusses the conclusions of this work related to above research questions and provides recommendations for further work. Lastly, Appendix A presents the verification and validation under taken for this thesis to show that the control algorithms are correctly implemented.

2

Journal Article

Control methods for geostationary debris removal using solar sailing

F.T. de Veld [*]

Delft University of Technology, Delft, 2628 CD, The Netherlands

This work considers active geostationary debris removal using solar-sail control. The usability of the analytical accessibility-and-deficit blending method for providing this solar-sail control is explored. This control method is compared with numerical methods from literature in terms of the resulting round-trip mission times as well as the relevant control parameters. Using a detailed dynamical model, it is shown that the outward transfers from a geostationary orbit to the graveyard orbit and inwards transfers back to a geostationary orbit obtained using different analytical control methods do not match with the results from literature obtained through numerical optimisation. Using initial conditions from literature, the trajectories obtained through analytical control result in mission times ranging from 630 to 760 days, which are a factor 1.4 to 5.1 larger compared to results from numerical control. This difference is due to changes in the semi-major axis and eccentricity during the transfer to the graveyard orbit using analytical control methods which are larger than required. Despite the discrepancy with literature, the analytical control methods could potentially be used for preliminary parameter space reduction. A sensitivity analysis of the mission time results shows an approximately exponential relationship with sail area, a strong seasonal coupling and little dependence on the debris mass. A case with both solar radiation pressure acceleration and solar electric propulsion acceleration is also analysed, demonstrating the large potential of solar electric propulsion for this mission case. Round-trip mission times resulting from the accessibility-and-deficit blending method can be halved from for example 765 days to 380 days, using SEP acceleration magnitudes of approximately 1% of the solar-sail characteristic acceleration.

---

[*]MSc Student, TU Delft Faculty of Aerospace Engineering, f.t.develd@student.tudelft.nl

Nomenclature

A	Area [m^2]		$S_{acc(k)}$	Accessibility score for orbital element k [-]
a	Semi-major axis [km]		$S_{def(k)}$	Deficit score for orbital element k [-]
a_c	Characteristic acceleration [m/s^2]		$\hat{s}_1, \hat{s}_2, \hat{s}_3$	First, second and third unit vector describing the Sun-sail reference frame
C_r	Reflectivity coefficient [-]			
$\hat{d}$	Projection vector of $\hat{n}$ on the $(\hat{s}_2, \hat{s}_3)$-plane		T_{SEP}	SEP thrust magnitude [N]
e	Eccentricity [-]		t	Time [s]
$\hat{e}_1, \hat{e}_2, \hat{e}_3$	First, second and third unit vectors describing the ECI reference frame		W_k	Weight function for orbital element k [-]
			α	Solar-sail cone angle [deg]
f, g, h, k, L	Second to sixth modified equinoctial orbital elements [L: deg]		$\tilde{\alpha}$	Ideal cone angle [deg]
			α^*	Optimised cone angle [deg]
h_a	Altitude [km]		β	Solar-sail lightness number [-]
I	Retrograde factor		γ	SEP thrust in-plane angle [deg]
I_{sp}	Specific impulse [s]		δ	Solar-sail clock angle [deg]
i	Inclination [deg]		ϵ	SEP thrust out-of-plane angle [deg]
$M_{W,a}$	Weight multiplier factor for W_a [-]		$\hat{\lambda}$	Ideal thrust direction
$M_{W,e}$	Weight multiplier factor for W_e [-]		μ	Gravitational parameter [km^3 s^{-2}]
m	Mass [kg]		ν	True anomaly [deg]
$\hat{n}$	Normal vector		σ	Sailcraft areal density [kg m^{-1}]
P	Solar radiation pressure at 1 AU [N/m^2]		ϕ	Latitude [deg]
p	Semi-latus rectum [km]		Ω	Longitude of the ascending node [deg]
r_p	Radius of pericenter [km]		ω	Argument of periapsis [deg]
$\hat{r}_1, \hat{r}_2, \hat{r}_3$	First, second and third unit vector describing the RTN reference frame		$\mathbb{1}_{Eclipse}$	Eclipse indicator function
			$\mathbb{1}_{inward}$	Inward transfer indicator function

2

I. Introduction

Solar sailing is an emerging space propulsion method in which thin, reflective membranes are employed to control the reflection of incoming solar radiation. The transfer of impulse from the photons can be of sufficient magnitude to result in a noticeable force, which can be controlled accordingly through active control of the membrane orientation with relation to the incoming sunlight. Using large area-to-mass ratios for the membranes, low-thrust propulsion similar to that of ion engines can be achieved, yet without consumption of any propellant. This advantage comes at a price of strict constraints on the magnitude and direction of the force acting on the sail, as it can never be directed towards the direction of sunlight and the solar radiation pressure (SRP) acceleration magnitude is strongly coupled with the direction. Despite these constraints, the characteristics of solar sails allow for unique trajectories and mission goals [1].

The application of solar sailing to real missions has a relatively short history, as the first demonstration mission IKAROS was successfully launched in 2010. A handful of additional missions have flown since then. However, solar-sail technology has improved significantly in this time period and the variety of theoretical research on the potential of solar sailing is coming closer to reality. The prospects of long-term acceleration and mission lifetimes not limited by propellant usage have inspired much research, including applications such as solar storm warning missions at an artificial Lagrange point [2] or interstellar probes [3]. A topic which has so far been rather underdeveloped is the usage of solar sails for space debris removal, especially repeatable removal.

Space debris is rapidly becoming an urgent problem for the space industry because of the collision risk it poses to active satellites. Space debris objects encompass objects as large as defunct satellites, but mostly small objects originating from various satellite and rocket body parts. As these debris objects are uncontrolled, poorly tracked, and can hit active satellites with velocities of multiple km/s, much attention is paid to the space debris situation to prevent collisions. Despite growing efforts however, the number of planned missions for active debris removal is still minimal. One of the first active debris removal missions is ClearSpace-1, scheduled to launch in 2025 for removing debris from LEO [4]. It is also speculated that the Chinese space agency has recently successfully attempted an active debris removal mission in the GEO region [5]. Despite these efforts, more work is needed especially for high-altitude orbital regions such as the geostationary belt, as debris left in this region will naturally de-orbit only after millions of years [6].

Since the IADC Space Debris Mitigation Guidelines have been put into place, the geostationary belt has become a protected orbital region in which satellites are not allowed to stay after their end-of-life [7]. There is a 25-year time frame for satellites to move out of this region, often to a so-called graveyard orbit positioned at a higher altitude than the protected region. Nevertheless, all satellites launched before these guidelines are still orbiting here in an uncontrolled manner. Furthermore, not all satellites manage to complete a successful end-of-life plan and there are no (legal) repercussions in case a defunct satellite does not move out of this protected region in time. Meanwhile, the risk of space debris collisions continues to increase. The geostationary (GEO) satellites Olympus-1, Express-AM11, AMC-9 and Telkom-1 satellites have all been hit by space debris and some of them have been rendered completely unusable [8–11].

3

A GEO debris removal mission would form an excellent application for solar sailing. Not only is the ratio of solar radiation pressure acceleration to other accelerations virtually maximum in GEO with relation to other Earth-centred orbits, but also the risk of sail damage due to small debris is relatively low. Another advantage is that this mission case lends itself for re-usability, which is easier to achieve using solar sailing than using other propulsion methods. Transfers from the GEO region to the graveyard orbit and back can be repeated many times, but are in practice often limited by the amount of propellant on-board of the satellite. This limitation is eliminated with solar sails.

The application of solar sailing to space debris removal is a niche field and most of the research is focused on 'passive' de-orbiting of satellites from low Earth orbit (LEO) or medium Earth orbit (MEO) to burn up in Earth's atmosphere, meaning that a solar sail is integrated in the satellite as an end-of-life plan, rather than in an external satellite [12] [13]. The control strategy often includes a method for constant eccentricity raising followed by an orientation to maximise drag. Especially for satellites in MEO this concept can be of interest because of the high ΔV required for de-orbiting. However, this concept does not easily allow for re-usability as the debris object burns up in the atmosphere together with the sail. There is less research on solar-sail assisted debris removal in GEO, but foundations have been laid by Kelly and Bevilacqua in a series of research articles about their TugSat concept, a 50 kg satellite with a sail area of 750 m^2 to capture objects up to 1000 kg, thus with a total area-to-mass ratio of 0.71 m^2/kg during the outward transfer to a graveyard orbit [14] [15]. Using multiple control strategies throughout their research, they manage to reduce the time for the outward transfer, orbit circularisation and inward transfer back to GEO from approximately 450 days in preliminary work [14] to approximately 150 days using Lyapunov control and particle swarm optimisation [15], with similar solar-sailing parameters in the same order of magnitude. Based on earlier works of Kelly and Bevilacqua which used pseudospectral methods, Mei et al. further developed their pseudospectral optimisation procedures for sail-assisted debris removal with the Legendre-Gauss-Lobatto (Open Loop) method [16]. Their work focuses more on the development of a non-linear controller based on pseudospectral methods than on finding minimum-time trajectories as their work is still in an early stage. They assume an area-to-mass ratio of 0.14 m^2/kg for the total structure during the outward transfer mission and find transfer times of approximately 350 days, roughly in line with the early results of Kelly and Bevilacqua [14]. However, Mei et al. do not investigate the return trajectory to GEO, which was found to be more time-consuming by Kelly and Bevilacqua [14].

Solar-sail control depends on the mission goals. For simple goals such as targeting one particular orbital element, locally optimal steering laws exist, which yield the ideal cone and clock angle for maximising the rate of change of this orbital element. Despite their simplicity, in cases like Earth-escape trajectories these analytical methods tend to result in excellent performance compared to numerical counterparts, requiring much less computational effort [1]. For more complex or constrained mission goals, numerical as well as analytical methods exist for finding optimal control variables. One such analytical method is called the 'accessibility-and-deficit ($A^n D$) blending method' developed by Macdonald and McInnes [17], designed for combining multiple objectives, such as targeting multiple orbital elements.

The applicability of the A^{n}D-blending method to repeatable GEO debris removal missions is investigated in this paper. This technique was developed in 2005 and since then many new control methods for solar sailing have been based on it. Examples include additions based on improving realism [18], the combination with numerical methods such as genetic algorithms [19] and usage of the A^{n}D blending method with non-ideal sails [20].

The objective of this paper is threefold: firstly, this work aims to assess whether analytical control methods result in minimum-time trajectories similar to numerical optimisation techniques from literature for re-orbiting GEO debris to a graveyard orbit and returning the sailcraft to GEO. Usage of analytical control allows reducing the computational load per analyses and thus a wider range of solar-sail parameters can be analysed. Secondly, the aim is to understand the sensitivity of minimum-time results to various mission parameters, such as debris mass, sail area and the mission time starting epoch. Lastly, this paper aims to understand the influence on the minimum-time results of additional solar electric propulsion (SEP) acceleration next to existing SRP acceleration. The extension to hybrid solar-sail/solar electric propulsion (SEP) thrust is performed to improve the performance of the GEO debris removal mission.

The remainder of this paper introduces the use case of this paper in section II and discusses the dynamics of this use case in section III. A theoretical background of the solar-sail control method used is given in section IV, with a focus on the A^{n}D blending method and an extension of the A^{n}D blending method into hybrid thrust. The tuning and validation of the A^{n}D blending method is discussed in section V. The mission time results are presented in section VI, both for the solar-sail only case for the extension to hybrid thrust in subsection VI.D. Lastly the conclusions are drawn in section VII.

II. Use case: GEO debris removal

This research focuses on trajectories from the GEO region to the graveyard orbit and back. The protected GEO region is defined by the Inter-Agency Space Debris Coordination Committee (IADC) through [21]:

$$0 \text{ deg} \leq \phi \leq 15 \text{ deg}$$

$$35586 \text{ km} \leq h_a \leq 35986 \text{ km}$$

where ϕ is the latitude and h_a is the altitude. This means that this protected region can be defined by the semi-major axis a, the eccentricity e and the inclination i only. Most of the objects in the GEO region have inclinations and eccentricities smaller than 10^{-4} and semi-major axes close to 42167 km [22]. The IADC guidelines mention that objects need to be removed from this region within 25 years after their end of mission [7]. All manoeuvres resulting in the object being outside this region after 25 years are permitted, but in practice moving the debris object to an orbit with a semi-major axis slightly larger than the one of the GEO semi-major axis is the most common technique. Sending a GEO object to a heliocentric orbit or letting it re-enter in Earth's atmosphere are more sustainable options, but in practice infeasible from an energy, time or reusability perspective [12].

5

The minimum requirement is for the pericenter $r_p = a(1 - e)$ of the GEO orbit of the debris object to be raised by [23]:

$$\Delta r_p = 235 \text{ km} + 1000 \frac{C_{r_d} A_d}{m_d} \text{km} \tag{1}$$

Δr_p is the change in pericenter radius and C_{r_d} and $\frac{A_d}{m_d}$ are the reflectivity coefficient and the area-to-mass ratio of the debris object respectively. Note that throughout this paper, the subscript $_d$ refers to debris-related properties. Badhwar et al. estimate the relation between A_d and m_d as follows [24]:

$$\tilde{m}_d = 37.97 \cdot \tilde{A}_d^{1.86} \tag{2}$$

where $\tilde{m}_d$ and $\tilde{A}_d$ are the average mass in kg and cross-sectional area in m^2 across all debris objects. The average is used because the standard deviation of these parameters is rather large for GEO objects [24]. However, this standard deviation decreases for larger debris mass values, which are the focus in this work. The vast majority of debris objects in GEO have masses in the order of one gram or less [21], which makes it impractical to remove these objects from GEO with a sailcraft with a mass of 500 kg, which is seen as a representative sailcraft mass [25]. Instead, debris objects with masses of 250 kg to 1000 kg are studied. Substituting these values in Eq. (2) results in area-to-mass ratios ranging from 0.006 m^2/kg for $m_d = 250$ kg to 0.02 m^2/kg for $m_d = 1000$ kg. A commonly used value for C_{r_d} is 1 [26], which results in a value Δr_p ranging from 235 to 245 km, see Eq. (1).

For most of the analyses of this paper, solar sailing is the main method of propulsion. Sail areas are assumed to be between 7500 and 15000 m^2, a significant scale-up compared to current-day sail areas of solar-sailing missions, of which IKAROS had the largest sail with an area of 196 m^2 [27]. To achieve similar sail acceleration levels as for mission that have already flown, the sail area needs to scale up due to the larger spacecraft mass and its payload, which includes the debris object. The sailcraft mass is assumed to be 500 kg [25], and the mass of the debris object ranges between 250 kg and 1000 kg in this paper. For comparison, the mass of the heaviest sailcraft IKAROS was 307 kg including payload [27]. The area-to-mass ratio of the sailcraft simulated in this work then lies between the ratios of flown missions and the ratios found in literature for the GEO debris removal use case [27]. For a part of the analysis, propulsion is assumed to be a hybrid between solar-sailing propulsion and SEP propulsion. The SEP engine is modelled after the BepiColombo SEP thrusters, which have a specific impulse of 4000 s and a maximum thrust of 149 mN. While the SEP acceleration magnitude is capped at 149 mN, in this work no SEP-thrust levels larger than 2.5 mN are used, based on preliminary results [28]. An overview of all mission parameters for the GEO use case can be found in Table 1. This table includes the target values for orbital parameters, meaning the final values of orbital elements at the end of a transfer. The variable values from Table 1 are used throughout the paper, except for validation test cases in subsection V.B.

Table 1   Constant simulation settings used throughout this paper

Parameter	Value	Parameter	Value
Initial orbital parameters	$a = 42167$ km, $e = 0$	Target value a inward transfer [km]	42167
Initial epoch t_0	June 21st, 2000	Target value e inward transfer [-]	0
Sailcraft mass (unloaded) [kg]	500	Specific impulse I_{sp} [s]	4000
Reflectivity coefficient debris C_{r_d}	1	Range of Δr_p [km]	235 - 245
Range of sail areas A [m^2]	7500 - 15000	Range of debris masses m_d [kg]	250 - 1000
Range of $\frac{A}{m}$ transfer out [m^2 kg^{-1}]	5 - 20	Range of $\frac{A}{m}$ transfer in [m^2 kg^{-1}]	15 - 30

III. Dynamics

The state of the sail is described in modified equinoctial orbital elements (MEOE) throughout integration and propagation. The MEOE set is based on the Kepler orbital elements a, e, i, the longitude of the ascending node Ω, the argument of periapsis ω and the true anomaly ν as follows [29]:

$$p = a(1 - e^2) \tag{3}$$

$$f = e \cos(\omega + I\Omega) \tag{4}$$

$$g = e \cos(\omega - I\Omega) \tag{5}$$

$$h = \tan\left(\frac{i}{2}\right)^I \cos(\Omega) \tag{6}$$

$$k = \tan\left(\frac{i}{2}\right)^I \sin(\Omega) \tag{7}$$

$$L = \omega + I\Omega + \nu \tag{8}$$

Here, p is the semi-latus rectum, $s^2 = 1 + h^2 + k^2$ and $w = 1 + f \cos(L) + g \sin(L)$ are shorthand notations and I is a so-called 'retrograde factor', which is equal to +1 for posigrade orbits and equal to -1 for retrograde orbits [29].

An advantage of the MEOE set is that it is nonsingular for all eccentricities and inclinations during propagation, contrary to the regular Keplerian set of orbital elements. Additionally, it has advantages compared to Cowell propagation with regard to computation efficiency for simulations including trajectories with slowly-changing orbital elements [30]. Throughout this research, MEOE propagation with an RK4 integrator using a time step of 50 s is used, following an analysis on the accuracy of the propagation of Eq. Equation 9.

States $\vec{X}$ are defined in the ECI reference frame $\mathcal{E}_{ECI}(\hat{e}_1, \hat{e}_2, \hat{e}_3)$, which is formally defined using three unit vectors $\hat{e}_1, \hat{e}_2$ and $\hat{e}_3$, with the frame origin at the centre of the Earth. The $\hat{e}_3$ unit vector points in the direction of the polar axis of the Earth and the $\hat{e}_1$-unit vector points towards the direction of the first point of Aries at J2000.0. The right-handed coordinate system is completed with the $\hat{e}_2$-vector in the equatorial plane [31]. $\vec{X}$ can be directly propagated using the equations of motion in Gaussian form [29]:

7

$$
\dot{\vec{X}} = \begin{bmatrix} \dot{p} \\ \dot{f} \\ \dot{g} \\ \dot{h} \\ \dot{k} \\ \dot{L} \end{bmatrix} = \begin{bmatrix} \dfrac{2pT}{w}\sqrt{\dfrac{p}{\mu_\oplus}} \\ \sqrt{\dfrac{p}{\mu_\oplus}}\left[S\sin(L) + \dfrac{((w+1)\cos(L)+f)T}{w} - \dfrac{g(h\sin(L)-k\cos(L))W}{w} \right] \\ \sqrt{\dfrac{p}{\mu_\oplus}}\left[-S\sin(L) + \dfrac{((w+1)\cos(L)+g)T}{w} - \dfrac{f(h\sin(L)-k\cos(L))W}{w} \right] \\ \sqrt{p}\mu_\oplus \dfrac{s^2 W}{2w}\cos(L) \\ \sqrt{p}\mu_\oplus \dfrac{s^2 W}{2w}\sin(L) \\ \sqrt{\mu_\oplus p}\left(\dfrac{w}{p}\right)^2 + \sqrt{\dfrac{p}{\mu_\oplus}}\dfrac{(h\sin(L)-k\cos L)W}{w} \end{bmatrix} \tag{9}
$$

S, T and W are perturbing acceleration components explained further in this section. $\mu_\oplus$ is the gravitational parameter for the Earth and its value can be found in Table 2. Dot-notation represents derivations with respect to time. The control variables are summarized in a vector $\vec{Y} = [\alpha,\ \delta,\ \gamma,\ \epsilon,\ T_{SEP}]$. α and δ are the sail cone and clock angles, respectively, providing the direction of SEP thrust (see subsection III.A for the definitions). γ and ϵ are two SEP thrust direction angles (see subsection III.D for the definitions) and T_{SEP} the SEP-thrust magnitude. Additionally, the spacecraft mass m is a relevant parameter for the state $\vec{X}$ as it changes instantaneously after the debris object is released and changes continuously during the propagations when using SEP thrust.

S, T and W are the components of the perturbing accelerations in the radial, transverse and normal directions respectively. Perturbing accelerations in this case refer to all accelerations which are not the acceleration caused by the point-mass gravity of the Earth. These perturbing accelerations are defined in a new reference frame, denoted by $\mathcal{E}_{RTN}(\hat{r}_1, \hat{r}_2, \hat{r}_3)$ with its origin at the sailcraft. The $\hat{r}_1$ unit vector points away from the centre of the mass of the Earth (radial direction). The $\hat{r}_3$ unit vector is oriented normal to the orbital plane of the sail (normal direction). The right-handed coordinate system is completed with the $\hat{r}_2$ unit vector (transverse direction), see Figure 1.
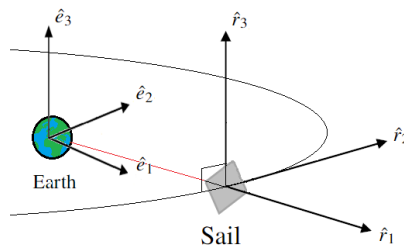
Fig. 1 The construction of the $\mathcal{E}_{RTN}$ frame for a sailcraft in a zero-inclination orbit around the Earth.

Referring to Figure 2, the main perturbing accelerations in the dynamical model at GEO altitude are, in order of magnitude, the acceleration caused by SRP, the acceleration due to the J_2-zonal harmonic and the point-mass gravity acceleration from the Moon and the Sun. Clearly, in case hybrid thrust is considered, the SEP acceleration also needs to
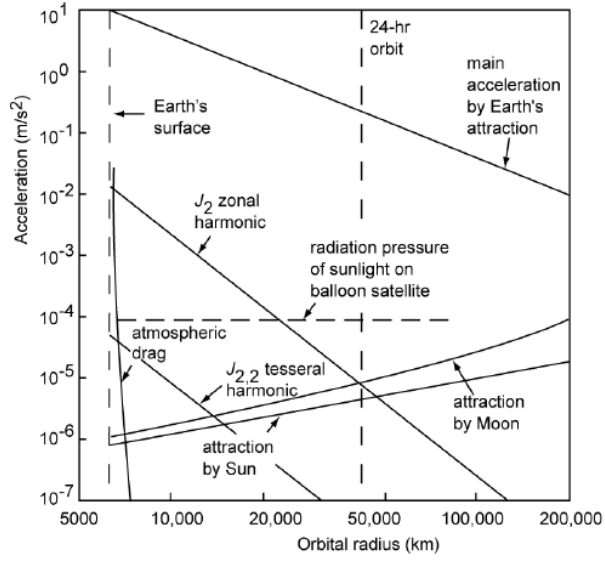
Fig. 2   Graph of the relative maximum magnitude of various perturbing accelerations as a function of the orbital radius, with GEO altitude marked by a dashed vertical line [31].

be accounted for. The sum of these perturbing accelerations appears in the equations of motions through the variables S, T and W. In the remainder of this section, the perturbing forces and all other vectors are described in the $\mathcal{E}_{ECI}$ frame, unless mentioned otherwise.

A. Solar radiation pressure

The solar-sail acceleration is modelled by assuming a flat and perfectly reflecting sail (i.e. ideal) model without wrinkles and degradation and without diffuse reflection and thermal emission, rather than an optical or more advanced model. It is known that this assumption can influence the time-of-flight results by up to 20% [32], yet as this paper serves as a preliminary study, this assumption is not prohibitive.

To define the SRP acceleration, a new reference frame $\mathcal{E}_{Sun-sail}(\hat{s}_1, \hat{s}_2, \hat{s}_3)$ is used with its origin at the sailcraft. The $\hat{s}_1$ unit vector points in the Sun-sail direction, $\hat{s}_2 = \hat{e}_3 \times \hat{s}_1$ and $\hat{s}_3$ completes the right-handed coordinate system [33], see also Figure 3. In case of ambiguities, the $\hat{s}_3$-vector is chosen such that the angle between the $\hat{s}_3$-vector of the $\mathcal{E}_{Sun-sail}$ reference frame and the $\hat{e}_3$-vector of the $\mathcal{E}_{ECI}$ reference frame is minimal.

9
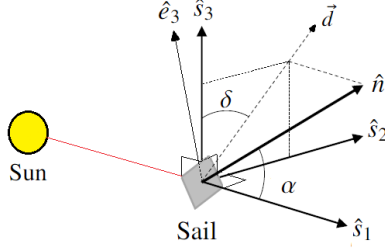
Fig. 3   An overview of the Sun-sail reference frame

To define the sail attitude in $\mathcal{E}_{Sun-sail}$, the cone angle α and the clock angle δ are defined. As can be seen from Figure 3, α is the angle between the $\hat{s}_1$-axis and the normal vector $\hat{n}$ and δ is the angle between the projection vector $\vec{d}$ of $\hat{n}$ on the $(\hat{s}_2, \hat{s}_3)$-plane of the $\mathcal{E}_{Sun-sail}$ reference frame and $\hat{s}_3$ of the same frame [33].

Following Figure 3, the normal vector $\vec{n}$ can be defined in the $\mathcal{E}_{Sun-sail}$ frame as:

$$\vec{n}^{\mathcal{E}_{Sun-sail}} = \begin{bmatrix} \cos(\alpha) \\ \sin(\alpha)\sin(\delta) \\ \sin(\alpha)\cos(\delta) \end{bmatrix} \tag{10}$$

As the solar radiation pressure is always directed away from the Sun, α must be confined to the interval $[-90, 90]$ deg. There is no such constraint for δ, which therefore has a width of 360 degrees and spans the interval $[-180, 180]$ deg.

For usage in the dynamical model, the normal vector $\vec{n}^{\mathcal{E}_{Sun-sail}}$ is transformed to the normal vector $\vec{n}^{\mathcal{E}_{ECI}}$ as follows:

$$\vec{n}^{\mathcal{E}_{ECI}} = \left[\hat{s}_1^{\mathcal{E}_{ECI},T} \hat{s}_2^{\mathcal{E}_{ECI},T} \hat{s}_3^{\mathcal{E}_{ECI},T} \right] \cdot \vec{n}^{\mathcal{E}_{Sun-sail}} \tag{11}$$

$\hat{s}_i^{\mathcal{E}_{ECI}}$ for $i = 1, 2, 3$ is the i-th unit vector of $\mathcal{E}_{Sun-sail}$ in the $\mathcal{E}_{ECI}$ frame. The acceleration caused by solar radiation pressure is then calculated as [27]:

$$\vec{a}_{SRP} = \beta \frac{\mu_\odot}{r_{Sun-sail}^2} \cos(\alpha)^2 \mathbb{1}_{Eclipse} \vec{n}^{\mathcal{E}_{ECI}} \tag{12}$$

$$\beta = \frac{2PR_{ES}^2}{\sigma \mu_\odot} \tag{13}$$

$$\sigma = \frac{m}{A} \tag{14}$$

Here, $\vec{a}_{SRP}$ is the SRP acceleration, β is the lightness number, $r_{Sun-sail}$ is the distance between the Sun and the

sailcraft and $\mu_\odot$ is the gravitational parameter of the Sun of which the value can be found in Table 2. $P = 4.56 \cdot 10^{-6}$ N m^{-2} is the solar radiation pressure at 1 AU [1], R_{ES} is the average distance between the Earth and the Sun equal to 1 AU and σ is the sailcraft areal density or the mass-to-area ratio with m the spacecraft mass and A the area of the sail. Lastly, $\mathbb{1}_{Eclipse}$ is an indicator function, equal to zero when the sailcraft is in eclipse and equal to one when it is not. The sailcraft is assumed to be in eclipse when the distance of the Earth or Moon to the Sun-sail line segment is smaller than their respective radius, see Table 2 for the values of these radii.

The lightness number β, as well as the characteristic acceleration $a_c = \frac{2P}{\sigma}$, the maximum possible solar-sail acceleration at 1 AU when $\alpha = 0$, are typical parameters indicating the capabilities of the solar sail. β ranges between $9.8 \cdot 10^{-4}$ and $1.1 \cdot 10^{-2}$ for existing solar-sail missions and a_c between $5.8 \cdot 10^{-6}$ and $6.3 \cdot 10^{-5}$ m s^{-1} [27]. The sail areas and debris masses from section II lead to ranges for β and a_c in a realistic order of magnitude for this paper, namely ranging from $7.7 \cdot 10^{-3}$ to $4.2 \cdot 10^{-2}$ for β and between $4.56 \cdot 10^{-5}$ m s^{-2} and $2.5 \cdot 10^{-4}$ m s^{-2} for a_c.

B. Lunar and solar point-mass gravity

The third-body perturbations from the Moon and the Sun respectively are modelled through the following equations [30]:

$$\vec{a}_{PMG_\mathbb{C}} = -\mu_\mathbb{C} \left(\frac{\vec{r}_{Sail} - \vec{r}_\mathbb{C}}{|\vec{r}_{Sail} - \vec{r}_\mathbb{C}|^3} + \frac{\vec{r}_\mathbb{C}}{|\vec{r}_\mathbb{C}|^3} \right) \tag{15}$$

$$\vec{a}_{PMG_\odot} = -\mu_\odot \left(\frac{\vec{r}_{Sail} - \vec{r}_\odot}{|\vec{r}_{Sail} - \vec{r}_\odot|^3} + \frac{\vec{r}_\odot}{|\vec{r}_\odot|^3} \right) \tag{16}$$

Here, $\vec{r}_\mathbb{C}$, $\vec{r}_\odot$ and $\vec{r}_{Sail}$ are the position vectors of the Moon, the Sun and the sail in the $\mathcal{E}_{ECI}$ frame respectively. The position vectors of the Sun and the Moon are obtained through two-body propagations of the Earth in the Earth-Sun system and the moon in the Moon-Earth system respectively. The value for the gravitational parameter of the Moon, $\mu_\mathbb{C}$ can be found in Table 2.

C. J_2-zonal harmonic

The J_2-zonal harmonic forms the most significant correction to the point-mass gravity model of the Earth. The perturbing acceleration $\vec{a}_{J_2}$ is described by the following equation [34]:

$$\vec{a}_{J_2} = -\frac{3\mu_\oplus J_2 R_\oplus^2}{2r_{Sail}^5} \begin{bmatrix} e_1(1 - 5\frac{e_3^2}{|\vec{r}_{Sail}|^2}) \\ e_2(1 - 5\frac{e_3^2}{|\vec{r}_{Sail}|^2}) \\ e_3(3 - 5\frac{e_3^2}{|\vec{r}_{Sail}|^2}) \end{bmatrix} \tag{17}$$

11

e_1, e_2 and e_3 are the first, second and third position coordinates in the $\mathcal{E}_{ECI}$ frame and r_{Sail} is the distance between the Earth and the sailcraft. J_2 is the value of the J$_2$-coefficient and $R_\oplus$ is the radius of the Earth, see Table 2 for their values.

D. Additional low-thrust acceleration

Additional low-thrust acceleration is modelled for the propagations in which the solar-sail propelled spacecraft also makes use of an SEP engine. This acceleration is described by [35]

$$\vec{a}_{SEP} = \frac{\vec{T}_{SEP}}{m} \tag{18}$$

where $\vec{T}_{SEP}$ is the controllable SEP-thrust vector. The change in mass due to propellant consumption is described by the following differential equation:

$$\dot{m} = -\frac{T_{SEP}}{I_{sp}g_0} = -\frac{m \cdot a_{SEP}}{I_{sp}g_0} \tag{19}$$

Here, I_{sp} is the specific impulse of the SEP engine and g_0 is the terrestrial gravity constant, see Table 2 [35]. The thrust angles γ and ϵ are defined analogously to the solar-sail angles in the $\mathcal{E}_{Sun-sail}$ frame, see Figure 4. γ is the angle between the $\hat{s}_1$-axis and $\vec{T}_{SEP}$, spanning the interval [-90, 90] deg and ϵ is the angle between the projection of $\vec{T}_{SEP}$ on the $(\hat{s}_2, \hat{s}_3)$-plane of the $\mathcal{E}_{Sun-sail}$ reference frame and $\hat{s}_3$ of the same frame, spanning the interval [-180, 180] deg.
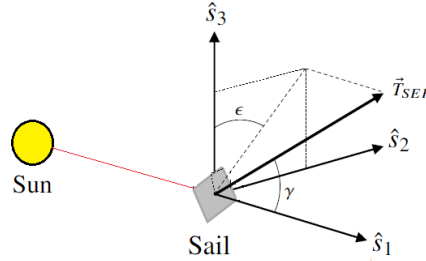
Fig. 4   Definition of the SEP-thrust angles γ and ϵ in the $\mathcal{E}_{Sun-sail}$ frame

Lastly, the equation for the spacecraft mass m at time t is as follows:

$$m(t) = m_{sail} + m_d \cdot \mathbb{1}_{inward} + \dot{m}t \tag{20}$$

Here, m_{sail} is the unloaded sailcraft mass and $\mathbb{1}_{inward}$ is an indicator function equal to zero when the current trajectory is an inward transfer to GEO and one when it is an outward transfer to a graveyard orbit.

The mass of the propellant at t_0 is not considered separate from the sailcraft mass for this work, since one year of

continuous SEP thrust of 2.5 mN would consume only 2.0 kg of propellant, following Eq. (19), which is very small compared to the assumed sailcraft mass of 500 kg. When the amount of required propellant becomes e.g. 10% of the sailcraft mass, for example during subsequent round-trip missions, the propellant mass should be considered during simulations.

Table 2 Physical constants used in the dynamical model [30] [36] [37]

Constant	Used value	Unit
$\mu_\oplus$	$3.98600441 \cdot 10^5$	km^3 s^{-2}
$\mu_\odot$	$1.32712440018 \cdot 10^{21}$	km^3 s^{-2}
$\mu_\mathbb{C}$	$4.9048695 \cdot 10^3$	km^3 s^{-2}
$R_\oplus$	$6.3781363 \cdot 10^3$	km
$R_\mathbb{C}$	$1.7374 \cdot 10^3$	km
g_0	9.80665	m s^{-2}

IV. Solar-sail control

Acceleration due to solar radiation pressure is one of the two accelerations in the dynamical model which can be controlled and the second one is the SEP acceleration, which is used only in part of the analysis. This section discusses the control methods for the two controllable accelerations which are used in this paper. The locally optimal steering laws for solar sailing are explained in subsection IV.A, as the A^{n}D blending method explained in subsection IV.B is based upon these. Another analytical control method called 'piecewise control' is discussed in subsection IV.C. Lastly, subsection IV.D discusses hybrid solar-sailing/SEP control.

A. Locally optimal steering laws

Locally optimal steering laws are control strategies to maximise the rate of change of an orbital element based on the variational equations. Locally optimal steering laws exist for any orbital element (except the true anomaly v) and any other parameter based on these orbital elements. In this paper, only the semi-major axis a, the eccentricity e and the radius of pericenter $r_p = a(1 - e)$ are of interest. While locally optimal steering laws for control lead only to a locally optimal solution, in instances such as finding Earth-escape trajectories, near-optimal results in terms of mission time can be obtained [1] [17].

The variation of any orbital element k can be written in a general form as [17]:

$$\frac{dk}{dt} = \vec{f_s} \cdot \vec{\lambda}_k \tag{21}$$

with k any orbital element, $\vec{f_s}$ the thrust vector and $\vec{\lambda}_k$ an ideal direction of thrust. Writing out Eq. (21) for a and e

13

results in the variational equations [38]:

$$\frac{da}{dt} = \frac{2a^2}{\sqrt{\mu_\oplus p}} [S\ T\ W] \cdot \begin{bmatrix} e\sin(\nu) \\ (1 + e\cos(\nu)) \\ 0 \end{bmatrix} \tag{22}$$

$$\frac{de}{dt} = \frac{|\vec{r}_{Sail}|^2}{\mu_\oplus} [S\ T\ W] \cdot \begin{bmatrix} \sin(\nu) \\ \frac{e\cos(\nu)^2 + e + 2\cos(\nu)}{1 + e\cos(\nu)} \\ 0 \end{bmatrix} \tag{23}$$

From Eq. (22) and Eq. (23) it can be seen that the perturbation acceleration components in the normal direction have no effect on the semi-major axis and eccentricity variations. Additionally, the rate of change $\frac{dk}{dt}$ is maximum when the perturbation vector $[S\ T\ W]$ points in the same direction as $\begin{bmatrix} e\sin(\nu) \\ (1 + e\cos(\nu)) \\ 0 \end{bmatrix}$ for a and $\begin{bmatrix} \sin(\nu) \\ \frac{e\cos(\nu)^2 + e + 2\cos(\nu)}{1 + e\cos(\nu)} \\ 0 \end{bmatrix}$ for e and their inner product is maximum. As such, the ideal thrust directions $\vec{\lambda}_a^{\mathcal{E}_{RTN}}$ for a and $\vec{\lambda}_e^{\mathcal{E}_{RTN}}$ for e are as follows:

$$\vec{\lambda}_a^{\mathcal{E}_{RTN}} = \begin{bmatrix} e\sin(\nu) \\ (1 + e\cos(\nu)) \\ 0 \end{bmatrix} \tag{24}$$

$$\vec{\lambda}_e^{\mathcal{E}_{RTN}} = \begin{bmatrix} \sin(\nu) \\ \frac{e\cos(\nu)^2 + e + 2\cos(\nu)}{1 + e\cos(\nu)} \\ 0 \end{bmatrix} \tag{25}$$

These vectors are defined in the $\mathcal{E}_{RTN}$ frame as is common in literature [1], [17]. Since the propagation is performed in MEOEs, it is convenient to express these ideal thrust directions in these elements, as well as $\vec{\lambda}_{r_p}$ [39]:

$$\vec{\lambda}_a^{\mathcal{E}_{RTN}} = \begin{bmatrix} f\sin(L) - g\cos(L) \\ 1 + f\cos L + g\sin L \\ 0 \end{bmatrix} \tag{26}$$

14

$$
\vec{\lambda}_e^{\mathcal{E}_{RTN}} = \begin{bmatrix} \dfrac{f\sin(L)-g\cos(L)}{\sqrt{f^2+g^2}} \\[2ex] \dfrac{\sqrt{f^2+g^2}+\cos\left(L-\tan^{-1}\left(\frac{g}{f}\right)\right)(2+f\cos(L)+g\sin(L))}{1+f\cos(L)+g\sin(L)} \\[2ex] 0 \end{bmatrix} \tag{27}
$$

$$
\vec{\lambda}_{r_p}^{\mathcal{E}_{RTN}} = \begin{bmatrix} (f\sin(L)-g\cos(L))\left(\dfrac{2\left(1-\sqrt{f^2+g^2}\right)}{1-f^2-g^2}-\sqrt{f^2+g^2}\right) \\[2ex] \dfrac{2\left(1-\sqrt{f^2+g^2}\right)(1+f\cos(L)+g\sin(L))}{1-f^2+g^2}-\left(\dfrac{f\cos(L)-g\sin(L)}{\sqrt{f^2+g^2}}+\cos(E)\right) \\[2ex] 0 \end{bmatrix} \tag{28}
$$

$\vec{\lambda}_k$ is a vector with its direction originating from the variational equations. Thus, maximising the component of $\vec{f}_s$ in the direction of $\vec{\lambda}_k$ is what maximises the rate of change of an orbital element k. When the orbital element k should be decreased instead, $\vec{\lambda}_k$ should be changed to $-\vec{\lambda}_k$ [17].

The ideal thrust direction $\vec{\lambda}$ can be used to determine solar-sail angles for locally optimal sail steering. To enable this, $\vec{\lambda}^{\mathcal{E}_{RTN}}$ is transformed to the $\mathcal{E}_{Sun-sail}$ frame and $\vec{\lambda}^{\mathcal{E}_{Sun-sail}} = [\lambda_{s_1}, \lambda_{s_2}, \lambda_{s_3}]$ is used instead. If the sail normal $\hat{n}$ pointed in the same direction as $\vec{\lambda}$, an ideal cone angle $\tilde{\alpha}$ and ideal clock angle $\tilde{\delta}$ could be extracted from $\vec{\lambda}$, see also their definition in Figure 3 in subsection III.A. The ideal cone angle $\tilde{\alpha}$ can then be obtained directly from $\vec{\lambda}^{\mathcal{E}_{Sun-sail}}$ through:

$$
\tilde{\alpha} = \text{sign}(\lambda_{s_2}) \cdot \cos^{-1}(\lambda_{s_1}) \tag{29}
$$

Note that the sign of $\tilde{\alpha}$ is equal to the sign of λ_{s_2} to allow for negative cone angles.

Sails cannot necessarily provide thrust in the direction of $\vec{\lambda}$ due to the solar-sail constraints on the cone angle and they do not provide equal thrust in all directions. $\hat{n}$ is therefore not necessarily equal to $\vec{\lambda}$ and an optimisation scheme based on maximising the inner product $\hat{n} \cdot \vec{\lambda}$ is used to optimise the component of $\vec{a}_{SRP}$ in the direction of $\vec{\lambda}$. An illustration of how an optimised cone angle α^* can be obtained through maximising the projection of $\hat{n}$ on $\vec{\lambda}$ is shown in Figure 5. This figure shows a contour in the $(\hat{s}_1, \hat{d})$-plane which indicates the SRP-acceleration magnitude for different cone angles, where $\hat{d}$ is the projection of $\hat{n}$ onto the $(\hat{s}_1, \hat{s}_2)$-plane as shown in Figure 3.
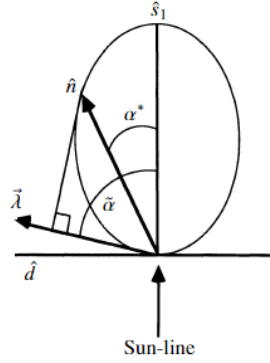
Fig. 5 **An illustration of how the optimised cone angle α^* is constructed from the ideal cone angle $\tilde{\alpha}$. Image adapted from McInnes (2004) [1].**

The optimisation scheme to compute an optimised cone angle α^* from an ideal cone angle $\tilde{\alpha}$ is as follows [1]:

$$\tan{(\alpha^*)} = \frac{-3 + \sqrt{9\cos{(\tilde{\alpha})^2} + 8\sin{(\tilde{\alpha})^2}}}{4\sin{(\tilde{\alpha})}} \tag{30}$$

The ideal clock angle $\tilde{\delta}$ can be found through [17]:

$$\tilde{\delta} = \cos^{-1}\left(\frac{\lambda_{s_3}}{\sqrt{\lambda_{s_2}^2 + \lambda_{s_1}^2}}\right) \tag{31}$$

The solar radiation pressure magnitude is independent from the clock angle and therefore $\tilde{\delta} = \delta^*$. [17].

1. Seasonal effects

The orientation of the position vector of the Sun with respect to $\vec{\lambda}_a$ and $\vec{\lambda}_e$ changes during the year. This can therefore lead to a seasonal variation in the cone and clock angles, which are defined with respect to the Sun-sail line. An illustration of the orientation of $\vec{\lambda}_a$ and $\vec{\lambda}_e$ in the $(\hat{e}_1, \hat{e}_2)$ plane in $\mathcal{E}_{ECI}$ during different seasons is shown in Figure 6 and Figure 7. This illustration is for the case $\Omega = \omega = i = 0$ deg, $e << 1$ and is not to scale. Note that when either a or e should be decreased instead, $\vec{\lambda}_a$ and $\vec{\lambda}_e$ flip direction.

It can be seen that the orientation of $\vec{\lambda}_a$ with respect to the Sun-sail vector $\vec{r}_{Sun-sail}$ displays no seasonal variation, only daily variation. $\vec{\lambda}_a$ is pointed towards the Sun as often as it is pointed away from the Sun, since the components of $\vec{\lambda}_a$ in $\mathcal{E}_{ECI}$ oscillate during one revolution around the Earth. However, the orientation of $\vec{\lambda}_e$ with respect to the Sun-sail vector does show seasonal variation. The orientation of $\vec{\lambda}_e$ in $\mathcal{E}_{ECI}$ is constant during one revolution around the Earth and as a result $\vec{\lambda}_e$ is pointed away from the Sun during the winter solstice, but is pointed towards the Sun during the summer solstice. Therefore, for $\Omega = \omega = i = 0$ deg, $e << 1$, $\vec{\lambda}_e$ leads to small cone angles during the winter solstice in a situation where the eccentricity should be increased, and during the summer solstice in a situation where
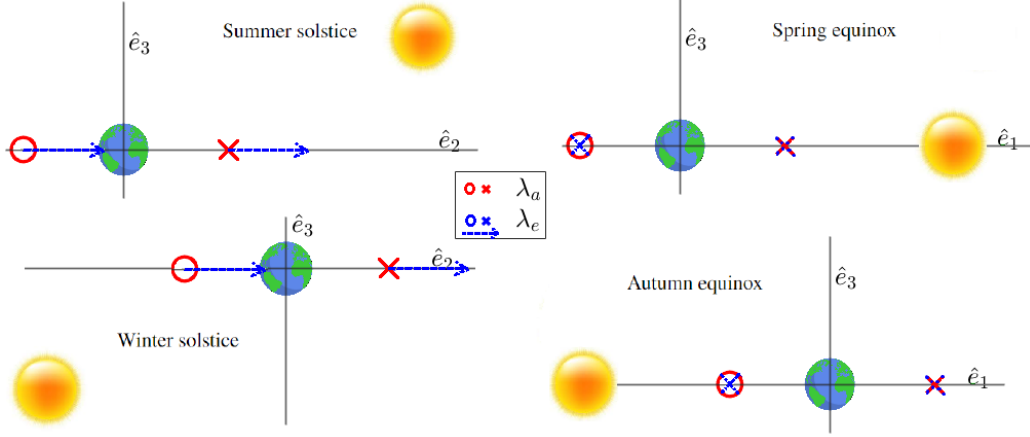
16
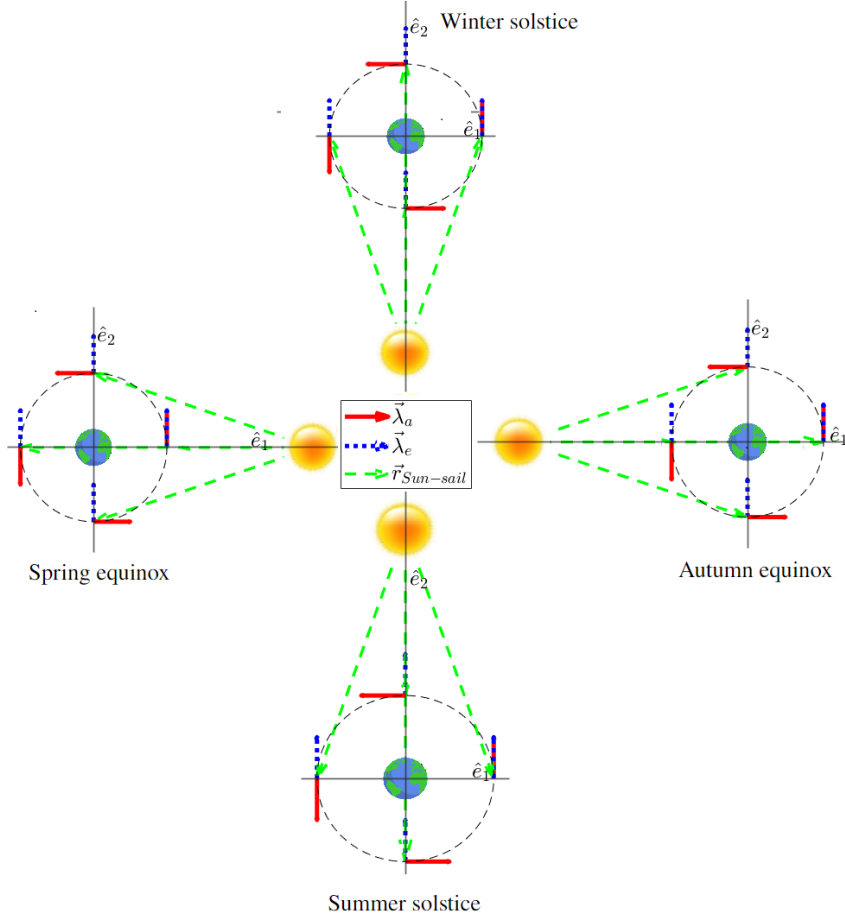
Fig. 6 The orientation of $\vec{\lambda}_a$ and $\vec{\lambda}_e$ with respect to the Sun in the $(\hat{e}_1, \hat{e}_2)$ plane in $\mathcal{E}_{ECI}$ for the summer solstice (bottom), autumn equinox (right), winter solstice (top) and spring equinox (left). Not to scale.

the eccentricity should be decreased.

The e_3-component of the Sun's position vector in $\mathcal{E}_{ECI}$ is not relevant during the equinoxes for $\Omega = \omega = i = 0$ deg, $e \ll 1$, as this component is zero. However, during the solstices it is relevant, since the Sun is then not located in the $(\hat{e}_1, \hat{e}_2)$ plane and neither is the Sun-sail vector. Therefore, $\vec{\lambda}_e$ is not pointed exactly towards the Sun during the summer solstice or away from the Sun during the winter solstice in the situation where the eccentricity should be increased. In that case, $\alpha < 90$ deg during the summer solstice and $\alpha > 0$ deg during the winter solstice and the e_3 component of the Sun's position vector decreases the seasonal effects.

When either Ω or ω increases, $\vec{\lambda}_e^{\mathcal{E}_{ECI}}$ rotates counterclockwise in the $(\hat{e}_1, \hat{e}_2)$ plane and the situation shown in Figure 6 occurs at an earlier time in the year, instead of the solstices and equinoxes. It is therefore difficult to make optimal use of the orientation of $\vec{\lambda}_e$ with respect to $\vec{r}_{Sun-sail}$.

Fig. 7 The orientation of $\vec{\lambda}_a$ and $\vec{\lambda}_e$ with respect to the Sun in the $(\hat{e}_1, \hat{e}_3)$ and $(\hat{e}_2, \hat{e}_3)$ planes in $\mathcal{E}_{ECI}$ for the solstices and equinoxes. A cross indicates an out-of-plane vector pointed away from the reader, a circle indicates an out-of-plane vector pointed towards the reader.

B. Accessibility-and-deficit blending method

Locally optimal steering laws are primarily meant for targeting one orbital element. When instead multiple orbital elements are targeted, each prescribing a different ideal thrust direction $\vec{\lambda}_k$, a method is needed to combine these directions into one direction which provides the cone angle α and clock angle δ for solar-sail control. A commonly used method is to average the ideal thrust directions based on weights, which can be defined in numerous ways. The accessibility-and-deficit (A^nD) blending method developed by Macdonald and McInnes is a fundamental example of such a blending technique [17].

With any number of ideal thrust directions for orbital elements, the blended ideal thrust direction $\vec{\lambda}_b^{\mathcal{E}_{Sun-sail}}$ is obtained as follows:

$$\vec{\lambda}_b^{\mathcal{E}_{Sun-sail}} = \frac{\sum_k W_k \vec{\lambda}_k^{\mathcal{E}_{Sun-sail}}}{|\sum_k W_k|} \tag{32}$$

where W_k denotes the weight function of the ideal thrust direction for changing orbital element k. By substituting $\vec{\lambda}_b^{\mathcal{E}_{Sun-sail}}$ into equations (29), (30) and (31), one optimised cone angle α^* and one optimised clock angle δ^* can be derived, which is the goal of the blending method.

The weight functions W_k from Eq. (32) indicate a form of priority for certain steering directions $\vec{\lambda}_k$, based on the sailcraft state. These weight functions are composed of two scores: an accessibility score and a deficit score. The accessibility score $S_{acc(k)}$ for the steering for an orbital element k is unique to solar sailing, as it represents the utilisation of the sail in terms of acceleration magnitude. The accessibility score is equal to [17]:

$$S_{acc(k)} = \cos{(\alpha_k^*)}^2 \tag{33}$$

Normalisation occurs with regard to the largest accessibility score, such that all individual accessibility scores are between zero and one. α_k^* is the optimised cone angle for changing an orbital element k. A larger accessibility score indicates a larger solar-sail acceleration magnitude and therefore a more efficient usage of the sail.

The deficit score instead is based on the rate of change of an orbital element k using optimised cone angles α_k^* and clock angles δ_k^* originating from an ideal thrust direction $\vec{\lambda}_k$. A longer required time to reach the target value leads to a larger deficiency score. The target values are the same as mentioned in section II. From the resulting angles, the direction of the sail normal $\hat{n}_k^{\mathcal{E}_{Sun-sail}}$ can be found using:

$$\hat{n}_k^{\mathcal{E}_{Sun-sail}} = \begin{bmatrix} \cos{(\alpha_k^*)} \\ \sin{(\alpha_k^*)}\sin{(\delta_k^*)} \\ \sin{(\delta_k^*)}\cos{(\delta_k^*)} \end{bmatrix} \tag{34}$$

Through a conversion of this vector into the $\mathcal{E}_{RTN}$ reference frame and multiplication with $a_c \cos{(\alpha_k^*)}^2$, the solar-sail acceleration $\vec{a}_{SRP}^{\mathcal{E}_{RTN}}$ can be found. Together with the other accelerations of the dynamical model as well as the mass, the thrust vector $\vec{f}_s$ can be found and Eq. (21) can be used to find the rate of change $\frac{dk}{dt}$. The deficit score $S_{def(k)}$ for the steering direction for an orbital element k is then defined as [17]:

$$S_{def(k)} = t_{end(k)} = \frac{k_{target} - k_t}{\frac{dk}{dt}} \tag{35}$$

with $t_{end(k)}$ the time required to reach the target orbital element k_{target} and k_t the value of an orbital element at the current time t. Like for the accessibility score, the deficit scores for the individual orbital elements are normalised according to the largest deficit score.

Following the method of Macdonald and McInnes, the normalised accessibility and deficit scores are added to form the weight functions W_k, resulting in a value between zero and two: $W_a = M_{W_a}(S_{acc(a)} + S_{def(a)})$ and $W_e = M_{W_e}(S_{acc(e)} + S_{def(e)})$. M_{W_a} and M_{W_e} are weight multiplier factors. Their usage is suggested by Macdonald and McInnes in case of a lacking performance of the A^{n}D blending method. These weight multiplier factors allow for better tuning of the solar-sail angles behaviour and can be found through a numerical analysis. In practice, tuning of these weight multiplier factors is often necessary when using the A^{n}D blending method [17]. The rationale behind summation of the accessibility and deficit scores instead of, for example, multiplication is that multiplication would give individual scores too much influence over the weight functions W_k, for example if one of the scores is zero [17]. From the weight functions W_k, one control vector $\vec{\lambda}_b^{\mathcal{E}_{Sun-sail}}$ can be found through Eq. (34).

19

There are a number of advantages and disadvantages of this A^nD blending method, originating from its characteristics. An advantage is that the calculations of the scores are only dependent on the current value of the orbital parameters and are independent of the time since the first epoch. This independence of time greatly simplifies the calculation process for the control, which speeds up the process of computing the solar-sail angles at each epoch compared to other control methods. Another advantage, which is particularly relevant for this work, is that the A^nD blending method allows blending of any locally optimal thrust direction $\vec{\lambda}_k$, which makes it comparatively easy to adapt the method to include SEP thrust control parameters. However, the optimality of the resulting solar-sail angles depends heavily on the method of blending the locally optimal steering vectors $\vec{\lambda}_k$, which is also noted by Macdonald and McInnes [17]. While the weight functions are already more robust than earlier work on Earth-escape trajectories, where they were defined based on simple exponential relationships [39], the weight functions of the A^nD blending method are still relatively simple and sensitive to (changing) input. Despite the inherent simplifications of the A^nD blending method, the method is applicable for on-board controllers, as the controller would be able to automatically correct for anomalies [17].

C. Piecewise control

To compare the performance of the A^nD blending method, another analytical method is defined for using multiple different locally optimal steering laws, namely *piecewise control*. With this control method, orbital parameters are targeted one by one, instead of at the same time like in the A^nD blending method. In the GEO use case of this paper, the semi-major axis and the eccentricity are targeted.

Using piecewise control, first the optimal steering direction for the semi-major axis $\vec{\lambda}_a$ is used for control until the semi-major axis target is reached and $|a - a_{target}| < T_{\text{inner(a)}}$ for a predefined inner tolerance level $T_{\text{inner(a)}}$. Then, the optimal steering direction for the eccentricity $\vec{\lambda}_e$ is employed until the eccentricity target is reached and $|e - e_{target}| < T_{\text{inner(e)}}$ for another predefined inner tolerance level $T_{\text{inner(e)}}$. When $|e - e_{target}| < T_{\text{inner(e)}}$ holds, it is checked whether $|a - a_{target}| < T_{\text{outer(a)}}$ still holds, with an outer tolerance level $T_{\text{outer(a)}} > T_{\text{inner(a)}}$. If this is not the case, the optimal steering direction for the semi-major axis $\vec{\lambda}_a$ is employed again for control until $|a - a_{target}| < T_{\text{inner(a)}}$. This procedure is followed iteratively until both $|a - a_{target}| < T_{\text{outer(a)}}$ and $|e - e_{target}| < T_{\text{outer(e)}}$.

D. Hybrid solar-sailing/SEP control

When considering hybrid solar-sailing/SEP control, it is useful to augment the acceleration contour for the SRP acceleration introduced in Figure 5 by adding the SEP acceleration to obtain the total acceleration contour. This augmentation is similar to the inclusion of the aerodynamic acceleration contour by Carzana et al. (2022) [33]. Since the SEP-acceleration magnitude is independent of the SEP-acceleration direction, adding the SEP-acceleration is equivalent to placing circles with their centre along each point of the SRP-acceleration contour and tracing the contour of the resulting figure, see Figure 8. The radius of these circles represents the SEP-acceleration magnitude $|\vec{a}_{SEP}|$.
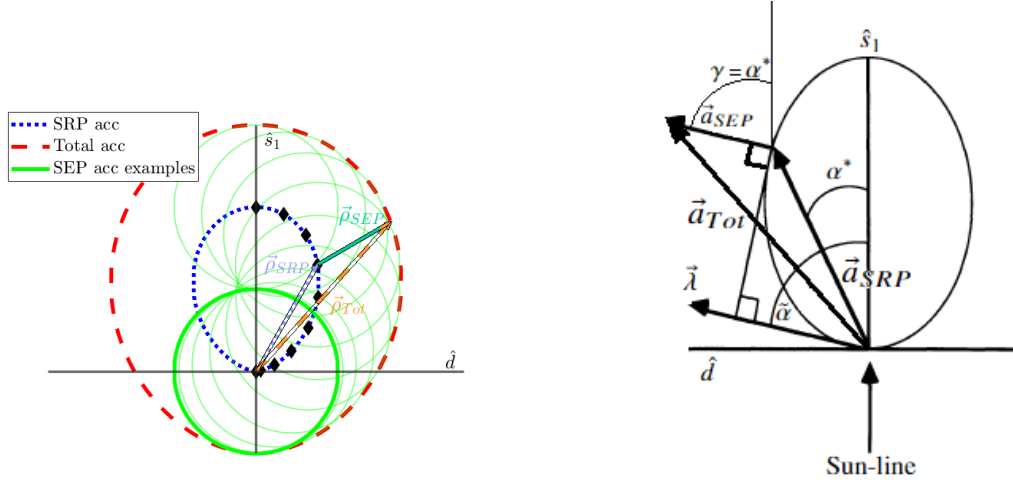
Fig. 8 **Construction of the total acceleration contour in dimensionless units (left) and visualisation of $\vec{a}_{SRP}$, $\vec{a}_{SEP}$ and $\vec{a}_{Tot}$ for a specific vector $\vec{\lambda}$ (right).**

Quantification of the total acceleration contour into an equation can be done through coordinate transformation. A position vector $\vec{\rho}_{SRP}$ can be defined in the $\mathcal{E}_{Sun-sail}$ frame, pointing to an arbitrary point (s_1, s_d) described by $s_1 = \sin(\alpha)\cos(\alpha)^2$ and $s_d = \cos(\alpha)^3$ on the SRP-acceleration contour. s_d is the coordinate of a vector in the $\mathcal{E}_{Sun-sail}$ frame along the $\hat{d}$-direction, see Figure 3. The total acceleration contour can be described in the $\mathcal{E}_{Sun-sail}$ frame through $\vec{\rho}_{Tot} = \vec{\rho}_{SRP} + \vec{\rho}_{SEP}$ pointing to a point (s'_1, s'_d), see Figure 8. $\vec{\rho}_{SEP}$ is a vector centred at (s_1, s_d) oriented perpendicular to the SRP-acceleration contour. The direction of $\vec{\rho}_{SEP}$ is described through the derivative $\frac{ds_d}{ds_1}$ of the SRP-acceleration contour as follows:

$$\vec{\rho}_{SEP} = \left[-\zeta \frac{ds_d}{d\alpha} \quad \zeta \frac{ds_1}{d\alpha} \right]^T \tag{36}$$

$$\zeta = \frac{|a|_{SEP}}{\sqrt{4\cos(x)^2 - 3\cos(x)^4}} \tag{37}$$

With this, $\vec{\rho}_{Tot}$ pointing to (s'_1, s'_d) is constructed as:

$$s'_1 = s_1 - \zeta \frac{ds_d}{d\alpha} = s_1 - \zeta(-3\sin(\alpha)\cos(\alpha)^2) = (3\zeta + 1)(\sin(\alpha)\cos(\alpha)^2) \tag{38}$$

$$s'_d = s_d + \zeta \frac{ds_1}{d\alpha} = s_d + \zeta(\cos(\alpha)^3 - 2\sin(\alpha)^2\cos(\alpha)) = (\zeta + 1)\cos(\alpha)^3 - 2\zeta\sin(\alpha)^2\cos(\alpha) \tag{39}$$

The total acceleration magnitude is then:

$$|\vec{a}_{tot}| = |\vec{\rho}_{Tot}| = \sqrt{s'^2_1 + s'^2_d} \tag{40}$$

The shape of the total acceleration contour is equal to the shape of the SRP-acceleration contour only for infinitesimal small SEP accelerations and is circular for infinitely large SEP accelerations. For other values, the shape is a blend between the shape of the SRP-acceleration contour and a circle. For SEP accelerations in the same order of magnitude as the SRP accelerations, the total acceleration contour has a shape very similar to the SRP-acceleration contour.

However, the total acceleration contour is not directly needed to determine the optimal control for the SEP acceleration when locally optimal steering laws are used. Maximising $\vec{\lambda} \cdot \vec{a}_{tot}$, the total acceleration component along the direction of $\vec{\lambda}$, leads to maximising $\vec{\lambda} \cdot (\vec{a}_{SRP} + \vec{a}_{SEP}) = \vec{\lambda} \cdot \vec{a}_{SRP} + \vec{\lambda} \cdot \vec{a}_{SEP}$. These terms can be maximised individually. The first term can be maximised following the optimisation procedure introduced in Eq. (30), while the second term directly leads to an SEP-thrust direction along the direction of $\vec{\lambda}$. This leads to $\gamma = \alpha^*$ and $\epsilon = \delta^*$, following their definitions given in subsection III.D. The total acceleration contour itself is thus not used further in this paper. Analogously to Figure 5, Figure 8 also shows a diagram showing $\vec{a}_{SRP}$, $\vec{a}_{SEP}$ and $\vec{a}_{Tot}$ for a specific vector $\vec{\lambda}$. Note that $\vec{a}_{SEP}$ is not parallel to $\vec{a}_{SRP}$.

V. Algorithm tuning and validation

This section presents the results of the tuning process for the A^{n}D blending method to the GEO use case of this paper in subsection V.A, as well as validation of single round-trip mission time results from the A^{n}D blending method with results from alternative control methods, both analytical and numerical, in subsection V.B. For all analyses, dynamical model settings from Table 1 are used unless otherwise mentioned. Integration is performed using an RK4 integrator with a fixed step size of 50 s, following an analysis based on integration errors for various step sizes. Computation of the control as well as the integration and propagation is performed on a personal CPU with an Intel(R) Core(TM) i7-6700 HQ CPU @ 2.60 GHz processor. Variable simulation settings for the different tuning and validation test cases can be found in Table 3. A mission is seen as finished when $|a - a_{\text{target}}| < 1$ km and $|e - e_{\text{target}}| < 5.0 \cdot 10^{-4}$.

A. Algorithm tuning and typical behaviour

As mentioned in subsection IV.B, before a quantitative analysis of the mission time results is presented, first the appropriate weight multiplier factors M_W for the semi-major axis weight function W_a and the eccentricity weight function W_e must be found to allow for optimal performance of the A^{n}D blending method [17]. These weight multiplier factors are multiplied by the A^{n}D blending weight functions W_k used in Eq. (32) to have more control over the weights for $\vec{\lambda}_k$, as defining the weights based on the accessibility and deficit score alone often does not yield the desired effect. Since there are only two weight functions, W_a and W_e, the weight multiplier factor for W_a can be defined with respect to the weight multiplier factor for W_e. If the weight multiplier factor for W_a has a value above one, the steering law for the semi-major axis gains more priority, while a value below one results in more priority for the steering law for the eccentricity.

22

Table 3 Variable simulation settings used for the tuning and validation test cases of this paper. Mass t_0 is the sum of the sailcraft mass and the debris object mass. [†]: initial time not mentioned in literature, Eq./sols.: equinoxes and solstices, *: literature also uses J_3-perturbation. Base: baseline dynamical model explained in this paper.

Setting	Tuning	Typical	Anal. comp.	Kelly (2017)	Kelly (2021)	Mei (2022)
Sail area [m^2]	15000	15000	15000	800	1200	140
Mass t_0 [kg]	500 + 500	500 + 500	500 + 500	50 + 1000	100 + 1100	500 + 500
Δr_P [km]	243	243	243	350	250	300
Out/in	Both	Both	Both	Both	Both	Out
Out β	0.023	0.023	0.023	0.0012	0.0015	0.0022
In β	0.046	0.046	0.046	0.025	0.019	-
T_{SEP} [mN]	0	0	0	0	0	0
t_0	June 21st, 2000	June 21st, 2000	June 21st, 2000	June 21st, 2000 [†]	Eq/sols. 2000 [†]	Jan 1st, 2017
a_{t_0} [km]	42 167	42 167	42 167	42 164	42 172	42 164
Dyn. model	Base	Base	Base	Base	Base	Base*
Propagator	RK4	RK4	RK4	RK4	RK4	RK4

For the two separate parts of the mission, outward and inward, only two different weight multiplier factors $M_{W,o}$ (outward) and $M_{W,i}$ (inward) are then used. Finding the optimal values for these two weight multiplier factors is done through a grid search and comparing the resulting mission times for a range of values for $M_{W,o}$ and $M_{W,i}$. Simulation settings for this weight multiplier factor analysis are found under the test case name "Tuning" in Table 3. The mission time results of the weight factor multiplier analysis are shown in Figure 9.
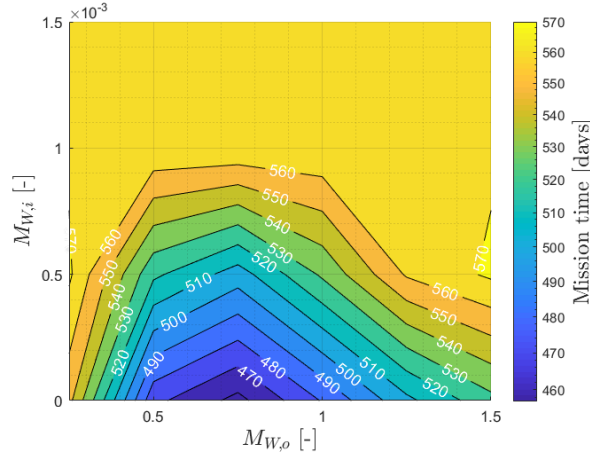

Fig. 9 Mission time as a function of the $M_{W,o}$ and $M_{W,i}$ for the semi-major axis weight

Figure 9, which uses grid sizes of 0.25 for the vertical and 0.0005 for the horizontal axis, shows that the mission time is dependent on both $M_{W,o}$ and $M_{W,i}$. It is found that values for $M_{WF,i}$ larger than 0.0015 do not result in convergence and the mission time shown in Figure 9 is equal to the maximum propagation time. It can be seen that $M_{W,o} = 0.75$ and

$M_{W,i} = 0$ are the optimal weight multiplier factors resulting in round-trip minimal time trajectories. A noteworthy result from Figure 9 is that the control during the inward transfer reduces to using a locally optimal steering law for the eccentricity. Further analysis with finer grids confirms these optimal values. The fact that results can be very dependent on algorithm tuning settings is not unexpected for the GEO use case, as Kelly and Bevilacqua noted that 10% of their simulations using numerically optimised control resulted in mission times longer than ten years, while mission times of one year were expected [14]. Weight multiplier factors $M_{W,o} = 0.75$ and $M_{W,i} = 0$ are used for all subsequent simulations using the A^{n}D blending method.

Next, the general behaviour of the orbital elements and solar-sail angles following usage of the A^{n}D blending control are analysed, as the behaviour of these parameters in the GEO use case is not known from literature. Simulation settings for this typical behaviour analysis are shown in Table 3 with the test case name "Typical". The behaviour of the semi-major axis and the eccentricity throughout the outward and inward transfers when A^{n}D blending control is used is shown in Figure 10.
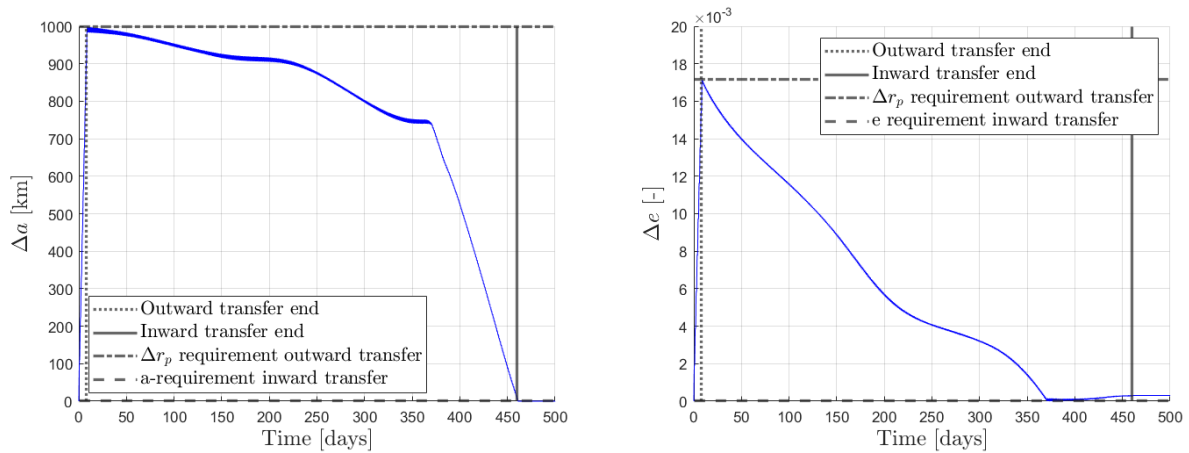

Fig. 10   Semi-major axis (left) and eccentricity (right) behaviour for a typical trajectory using A^{n}D blending control

These figures show the change of the semi-major axis and the eccentricity over time, as well as the parameter boundary conditions for the outward and inward transfer and the end moment of the outward and inward transfers. It can be seen that the outward transfer takes much less time than the inward transfer. This result shows that it is much quicker to increase the semi-major axis and the eccentricity using A^{n}D blending control than to decrease these parameters. Note that the round-trip mission time in Figure 10 is 460 days, equal to the optimal value in Figure 9. The oscillations visible in Figure 10 are due to seasonal variation in the steering direction $\vec{\lambda}_b$. This phenomenon is further discussed in subsection VI.A. Figure 10 shows one round-trip mission, though once GEO has been reached and a new debris

object has been targeted, another outward transfer could be started. The mission time per round-trip can be significantly reduced when the target value for the eccentricity for the GEO region is for example 0.005 instead of 0, as decreasing the eccentricity is a time-consuming process with A^nD blending control. However, as mentioned in section II, most debris objects have orbits with eccentricities smaller than 0.0005.

The typical behaviour of the cone angle α and clock angle δ with A^nD blending control is shown in Figure 11. This figure shows the behaviour in the intervals [4,5] days for the outward transfer and [290,291] days for the inward transfer, which is seen as representative.
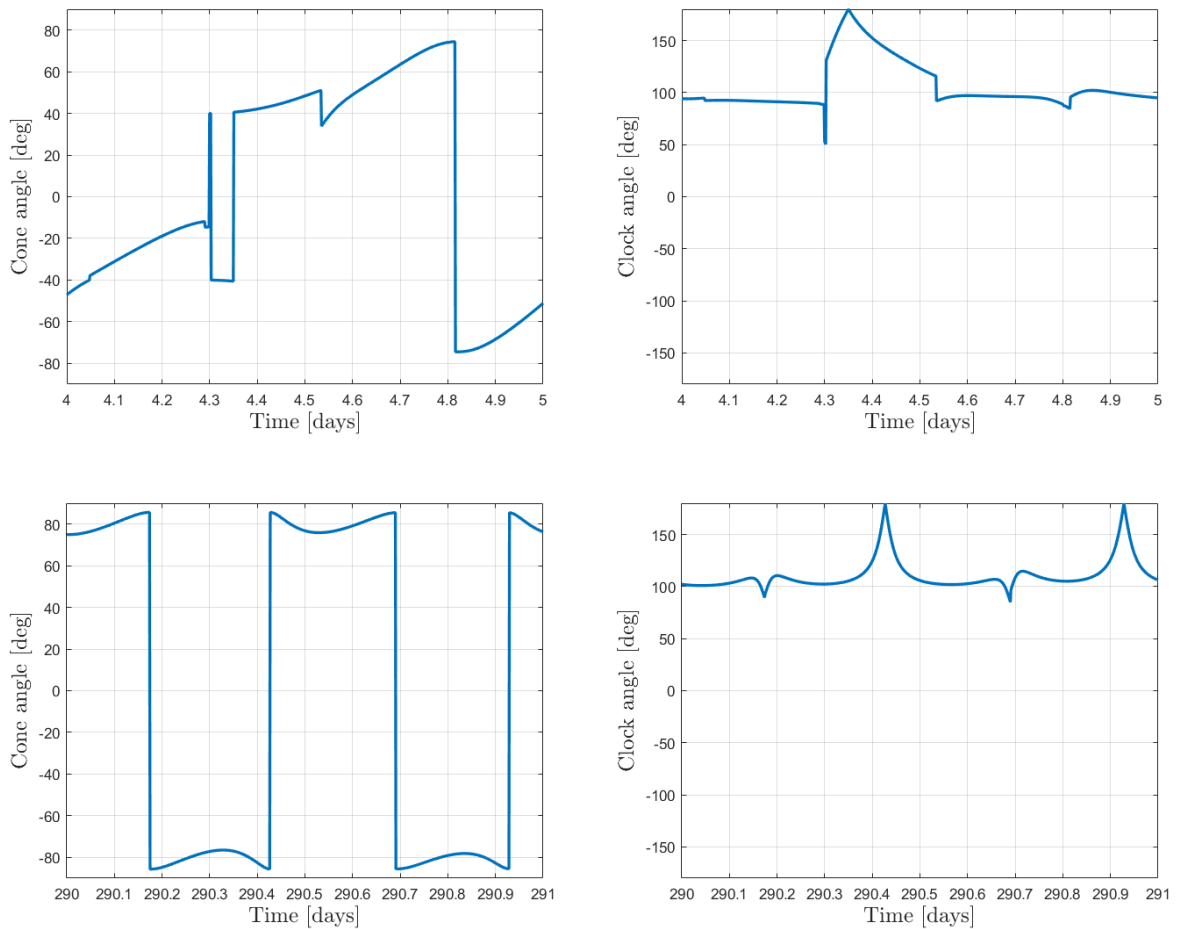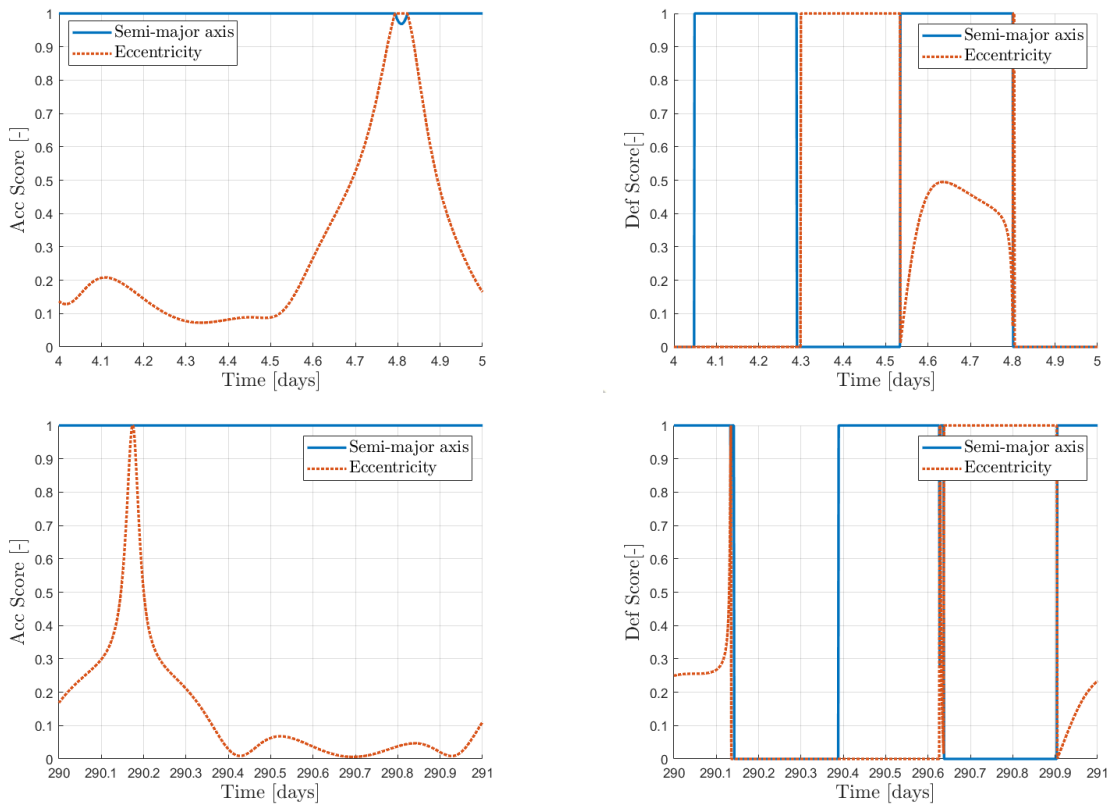

Fig. 11   Cone angles (left) and clock angles (right) for a typical outward (top) and inward (bottom) transfer using A^nD blending control, zoomed into the [4-5]-day (outward transfer) and [290-291]-day (inward transfer) intervals

It can be seen that both solar-sail angles change periodically over the course of approximately one day during the inward transfer, or equivalently one revolution. There is no periodic behaviour visible during the outward transfer. At some moments during the inward transfer, there are quick changes in the solar-sail angles. Here, the A^nD scores

$S_{acc,e}$ and $S_{def,e}$ rapidly change due to changes in the dynamics, namely daily variation in the difference between the ideal cone angle $\tilde{\alpha}$ and the optimised cone angle α^*. Figure 11 shows that the locally optimal steering law for the eccentricity results in large cone angles α, as the absolute value averages 80 deg. Large cone angles like these lead to a small resulting SRP-acceleration.

Lastly, Figure 12 shows the accessibility and deficit scores for the semi-major axis and the eccentricity for the time interval 290-291 days. Note that $M_{W,i} = 0$ and the A^{n}D scores for the semi-major axis have no influence on the control during this time interval.

Fig. 12 Accessibility (left) and deficit scores (right) for a typical outward (top) and inward (bottom) transfer using A^{n}D blending control, zoomed into the [4-5]-day (outward transfer) and [290-291]-day (inward transfer) intervals

The accessibility score shows a differentiable behaviour for both the semi-major axis and the eccentricity. The deficit score however shows several non-differentiable parts during the given time interval. These events occur when the rate of change $\frac{dk}{dt}$ of an orbital element k is zero while calculating the deficit score. When this situation occurs for the eccentricity, the control resulting from the A^{n}D blending method does not lead to the desired change in the eccentricity.

This result can be explained using Figure 13. The accessibility score for the eccentricity shown in Figure 12 reaches much smaller values than the accessibility score for the semi-major axis. This result can be explained through the direction of $\vec{\lambda}_e$, which results in $|\tilde{\alpha}_e| > 90$ deg during most of the inward transfer. Following the optimisation procedure of Eq. (30), the magnitude of the optimised cone angle $|\alpha_e^*|$ is then close to 90 deg. For $\vec{\lambda}_a$ it holds that $|\tilde{\alpha}_a| < 90$ deg and $|\alpha_a^*| < |\alpha_e^*|$. The large difference between $|\tilde{\alpha}_a|$ and $|\tilde{\alpha}_e|$ results in a similar difference between $S_{acc,a} = \cos(\alpha_a^*)^2$ and $S_{acc,e} = \cos(\alpha_e^*)^2$.
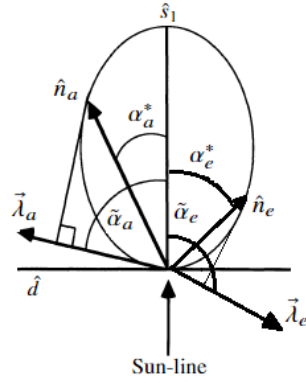
Fig. 13   Illustration how different directions for $\vec{\lambda}_a$ and $\vec{\lambda}_e$ can lead to different SRP-acceleration magnitudes. Image adapted from McInnes (2004) [1].

B. Validation

As one of the aims of the paper is to assess the usability of the A^{n}D blending method to the GEO use case, comparison of the mission time results from the A^{n}D blending with mission time results from literature is performed, as well as with mission time results for other analytical control methods described in section IV. This is done through reproduction of specific test cases.

1. Comparison with other analytical control methods

In section IV, two analytical control methods have been discussed which could form an alternative to the A^{n}D blending method, namely piecewise control and usage of the locally optimal control law for the pericenter radius increase, the latter only during the outward transfer. These control strategies are used to generate outward and inward transfers and the resulting mission times are compared with the ones from the A^{n}D blending method. Simulation settings can be found in Table 3 under the name "Anal. comp.". These settings are identical to the ones for the A^{n}D blending algorithm tuning. The behaviour of the semi-major axis and the eccentricity for the A^{n}D blending control can be seen in Figure 10.

Usage of the locally optimal steering law for the pericenter during the outward transfer yields identical results to

Figure 10. The overlap of results indicates that the control strategy of the A^nD blending method leads to the quickest possible increase for the pericenter during the outward transfer using analytical control, which is the result of tuning the weight multiplication factor $M_{W,o}$.

Piecewise control, introduced in subsection IV.C, can be used for both outward and inward transfers. Outer tolerances of $T_{outer(a)} = 1$ km and $T_{outer(e)} = 1 \cdot 10^{-4}$ and inner tolerances $T_{inner(a)} = 0.1$ km and $T_{inner(e)} = 1 \cdot 10^{-5}$ are used for the analytical comparison test case. The typical behaviour of the semi-major axis and the eccentricity using piecewise control in the GEO use case is shown in Figure 14. Note that the semi-major axis and the eccentricity show a continuous behaviour throughout the trajectory, though these elements occasionally change rapidly over time.
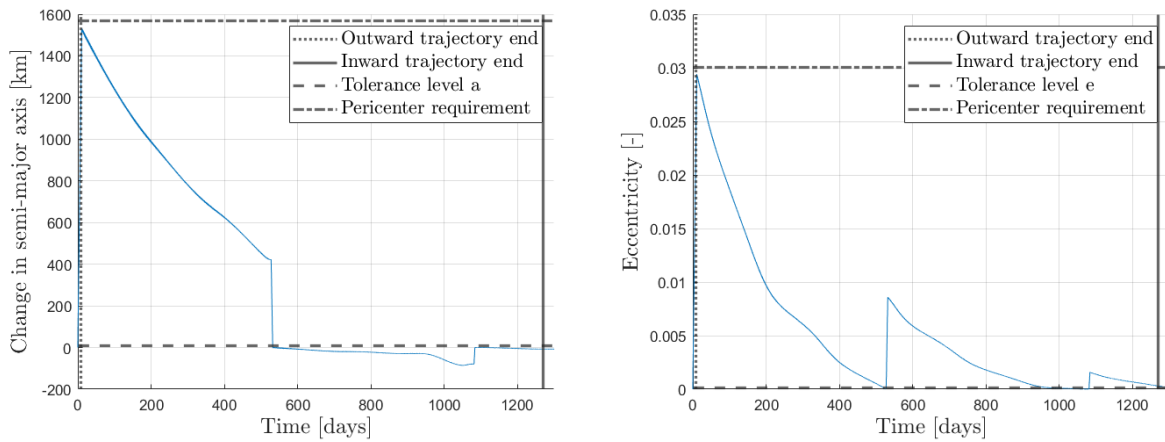
Fig. 14   Semi-major axis (left) and eccentricity (right) behaviour when piecewise control is applied

The outward transfer is completed within ten days, but the inward transfer takes almost 1300 days which is much more than the 460 days shown in Figure 10 obtained with the A^nD blending method with the same simulation settings. During most of the inward transfer, the eccentricity steering law is applied, resulting in overshooting in the sense that the semi-major axis decrease below the semi-major axis for GEO orbits. Another reason for the difference in mission times is that the piecewise control results in larger semi-major axis and eccentricity values when the outward transfer finishes compared to the A^nD blending results. Therefore, it takes more time to reduce these relatively large values back to the target values for the inward transfer.

### 2. Comparison with numerical control methods from literature

In literature, three test cases for GEO debris removal using solar sailing exist, using various numerical optimisation techniques for finding minimum-time trajectories for the round-trip mission. Specifics regarding these three validation test cases from literature can be found in Table 3. The first validation test case from literature analysed in this paper is

from the work of Kelly (2017) [14], where Lyapunov control is used for optimisation. The second validation test case from literature concerns the work of Kelly (2021) [15], where numerical control is much improved through a Gaussian quadrature implicit integration method with collation applied at Legendre-Gauss-Radau points. Numerical optimisation is then performed using SNOPT, a sparse nonlinear programming software package [15]. Both these validation test cases from Kelly assume much smaller sailcraft masses than what is currently feasible. The third validation test case from literature is from the work of Mei (2022) [16], where only the outward transfer to the graveyard orbit is discussed. Pseudospectral control techniques are applied for trajectory optimisation and mission parameters which are possible with current-day technology are used in the modelling. Validation test cases use the simulation settings from Table 1, unless mentioned otherwise in Table 3.

The A^nD blending method is applied to reproduce these three validation test cases from literature. The mission times resulting from the A^nD blending method are then compared to values from literature to understand how well the A^nD blending method performs for finding minimum-time trajectories. Additionally, the behaviour of control parameters and orbital elements throughout the mission are compared wherever possible. All results are compared in Table 5 at the end of this section.

The propagated results for the reproduction of the validation test case of Kelly (2017) are shown in Figure 15, comparing the behaviour of the semi-major axis and the eccentricity originating from A^nD blending control with those from Kelly (2017) [14]. Note that for neither the A^nD blending control nor the results from Kelly (2017), a zero eccentricity is reached at the end of the mission. The behaviour of the orbital elements throughout the mission using A^nD blending control is very different from the results from Kelly (2017), since no orbit circularisation at the graveyard orbit takes place using A^nD blending control and orbital element oscillations are smaller compared to the results from Kelly (2017). It can be seen that the Lyapunov control of Kelly results in shorter mission times, as the end of the inward transfer is reached within 450 days, while this takes 640 days with the A^nD blending control. One reason why the mission times are different is that the A^nD blending control leads to a larger change in the semi-major axis and the eccentricity than with the control from Kelly (2017). However, the semi-major axis and eccentricity values lead to the same pericenter value for both the A^nD reproduction as the results from Kelly (2017), see also Table 3, but it takes much time to decrease these parameters again. Unfortunately, Kelly and Bevilacqua did not share the cone and clock angle profiles for this test case, which makes further in-depth validation difficult.

For the validation test case of Kelly (2021) [15], the total mission time composed of an outward and inward transfer takes approximately 150 days, which is much less than the results of Kelly (2017) despite a smaller lightness number during the inward transfer for the case of Kelly (2021) [14]. Table 3 shows the simulation settings for this test case. The outward transfer takes 90 days, while the inward transfer takes 60 days. There is a seasonal effect visible on the mission time results [15].
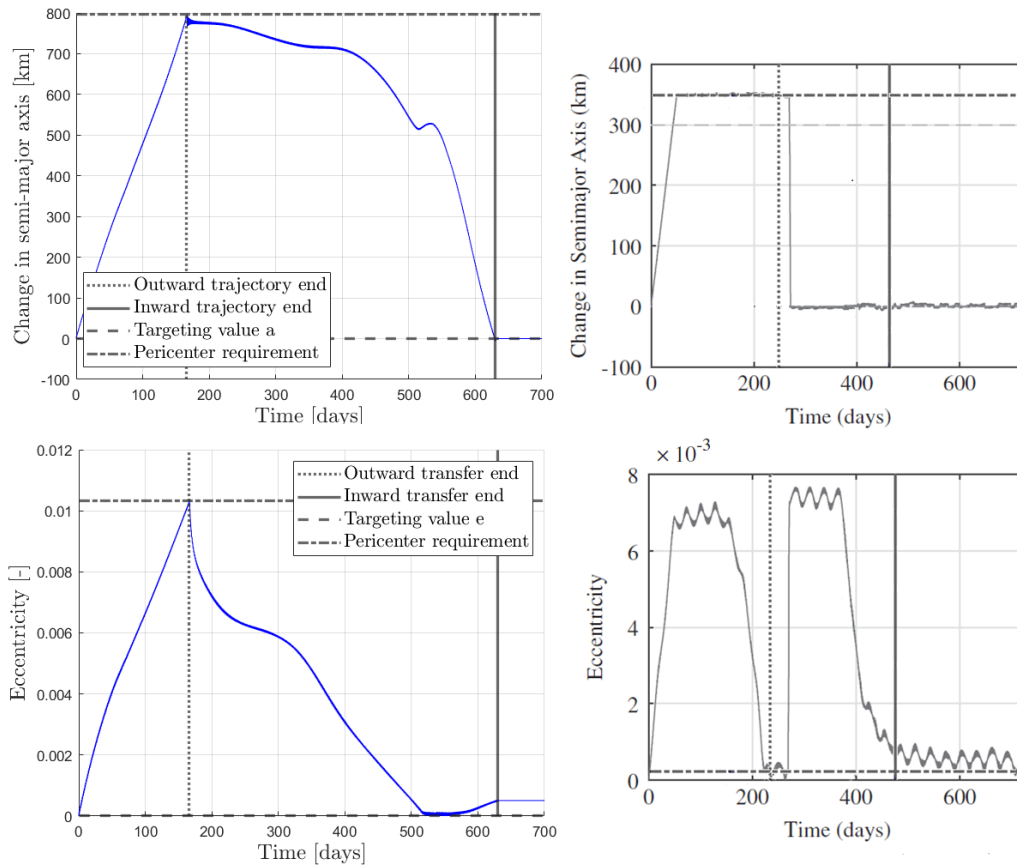
Fig. 15 Behaviour of relevant orbital elements for the reproduced test case with A^{n}D blending control (left) and from literature (right), for the study of Kelly (2017) [14]

The behaviour of the orbital parameters and solar-sail angles using A^{n}D blending control for the test case reproduction of Kelly (2021) is very similar to the behaviour seen for the test case reproduction of Kelly (2017) and is therefore not shown separately. The mission times for different mission starting dates are shown in Table 4. The average mission time obtained using A^{n}D blending control is 758.5 days, 5.1 times more than with the numerical control of Kelly (2021) [15]. Note that the variation in mission times in the results from Kelly (2021) is approximately 3% for different mission start dates, but this variation is 20% for the results from the A^{n}D blending method.

Thirdly, a comparison is performed with the results from Mei (2022) [16]. Simulation settings can be found in Table 3. Their numerical control results in an outward transfer time of 350 days, reaching an eccentricity of 0.006 in the graveyard orbit. A comparison between A^{n}D blending control and literature for the semi-major axis and eccentricity results is shown in Figure 16. Note that the first 20 days are cut off in the graphs from Mei (2022), as their optimisation method shows poor convergence in this region [16]. The control of Mei (2022) makes it possible to raise the semi-major axis nearly linearly while keeping the eccentricity below 0.003. However, eccentricity values below $5 \cdot 10^{-4}$ are not

Table 4 Mission times for different mission starting dates for the test case of Kelly (2021) [15]. All values are in days. The inward transfer time for Kelly (2021) averaged 59 days.
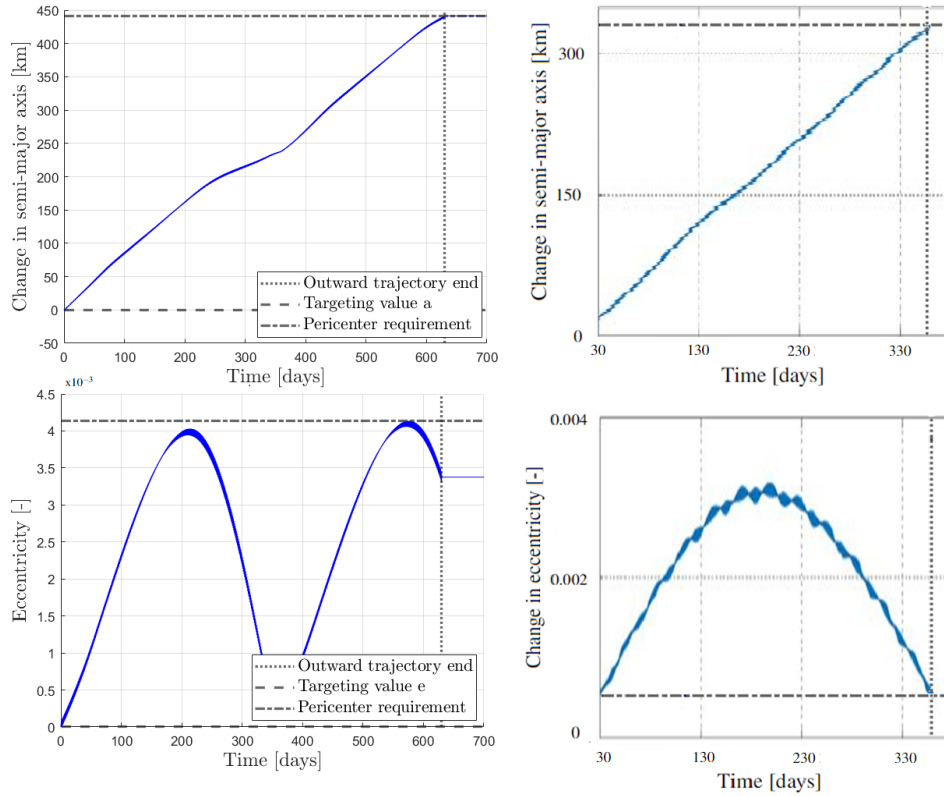
Initial date	Outward transfer time Kelly (2021)	Outward transfer time A^{n}D	Total mission time A^{n}D
Spring equinox	90.07	122.9	838.8
Summer solstice	93.30	100.2	611.7
Autumn equinox	89.10	101.9	753.4
Winter solstice	87.83	152.4	830.0
Average	90.00	119.4	758.5

reached in the results from Mei (2022) due to controller instability, while a zero eccentricity is targeted. The outward transfer takes 350 days [16]. It takes approximately 625 days for the A^{n}D blending control algorithm to complete the outward transfer, approximately 1.8 times longer compared to the mission times from Mei (2022). Like for previous validation test cases, the A^{n}D blending method reproduction shows semi-major axis and eccentricity values which are larger than in the case of Mei (2022). However, the eccentricity shows a different behaviour than for other test cases, as near-zero values are reached during the outward transfer. This result is caused by the fact that the outward transfer takes much more time than for previous test cases, and near the autumn equinox the eccentricity steering law results in much larger A^{n}D scores than in other seasons, which changes the control. This phenomenon is discussed in more detail in subsection VI.A.

The cone and clock angles are also given in the research of Mei (2022), though the cone angle α in their work is defined in the interval $[0, 90]$ deg instead of $[-90, 90]$ deg of this work. Following a conversion of the cone angles, it is found that $|\alpha|$ is on average approximately 40 deg for Mei (2022), but approximately 61 deg for results with the A^{n}D blending control. This difference in average $|\alpha|$ results in an average value for $|a_{SRP}|$ which is a factor 2.3 larger for the research of Mei (2022) than for the A^{n}D reproduction following Eq. (12). This difference in $|a_{SRP}|$ is influential for understanding the difference in mission time between literature and the A^{n}D reproduction.

Table 5 Results from literature compared with results from the A^{n}D blending method [14–16]. Reprod.: reproduction

Parameter	Kelly (2017)	Reprod.	Kelly (2021)	Reprod.	Mei (2022)	Reprod.
Max Δa [km]	350	800	390	780	305	445
Max Δe [-]	$7.8 \cdot 10^{-3}$	$1.0 \cdot 10^{-2}$	$3.2 \cdot 10^{-3}$	$1.2 \cdot 10^{-2}$	$3.0 \cdot 10^{-3}$	$4.2 \cdot 10^{-3}$
Δr_p [km]	350	350	250	250	300	300
Transfer time (out) [days]	220	165	90	119	350	625
Transfer time (in) [days]	250	465	60	640	-	-
Transfer time (tot) [days]	450	630	150	759	350	625
Factor difference w. literature	-	1.4	-	5.1	-	1.8

Fig. 16   Behaviour of relevant orbital elements for the reproduced test case with A^nD blending control (left) and from literature (right), for the study of Mei (2022) [16]

The factor difference with literature shown in Table 5 is significantly different among the test case reproductions. However, this difference is partially due to the usage of different numerical optimisation techniques in literature as well as the usage of different pericenter boundary conditions for the different test cases. The sensitivity of mission time results using the A^nD blending control to mission parameters is further discussed in section VI.

For the analysis further in this work, it can be concluded that the A^nD blending method is not as well suited as numerical control from literature for finding minimum-time trajectories for the GEO use case described in this paper.

VI. Results

This section discusses the results of using the A^nD blending method to obtain mission times for the GEO use case discussed in this paper. A sensitivity analysis of the mission time results for various mission parameters is presented, namely the time of the initial epoch, the sail area, the debris mass and the SEP acceleration magnitude. Table 6 shows the simulation settings for the simulations of this section.

Table 6 Variable simulation settings used for the test cases throughout this paper. Mass t_0 is the sum of the sailcraft mass and the debris object mass. Base: baseline dynamical model explained in this paper, sol.: solstices, eq.: equinoxes.

Setting	Seasonal sensitivity	Sail area sensitivity	Debris mass sensitivity	SEP acceleration sensitivity
Sail area [m^2]	15000	7500 to 15000	7500 to 15000	7500 to 15000
Mass t_0 [kg]	500 + 500	500 + 500	500 + 250 to 1000	500 + 500
Δr_p [km]	243	243	241 to 246	243
Out/in	Both	Both	Both	Both
Out β	0.023	0.012 to 0.023	0.0058 to 0.023	0.012 to 0.023
In β	0.046	0.023 to 0.046	0.023 to 0.046	0.023 to 0.046
T_{SEP} [mN]	0	0	0	0 to 2.5
t_0	Jan 1st - Dec 30th 2000	Sol. + Eq. in 2000	June 21st/Sep 22nd 2000	Jan 1st - Dec 30th 2000
Dyn. model	Base	Base	Base	Base
Propagator	RK4	RK4	RK4	RK4

A. Seasonal Variation

As mentioned in subsubsection IV.A.1, the control originating from the locally optimal steering law for *e* shows a seasonal dependence. This seasonal effect is visible in earlier test cases as a non-constant decrease of the eccentricity and semi-major axis. The sensitivity of the mission time results on the seasonal variation is analysed by repeating the baseline simulation resulting from the tuning of the $A^n D$ blending method for a range of times for the initial epoch. The simulation settings can be found in Table 6 under the name "Seasonal sensitivity". The results are shown in Figure 17.
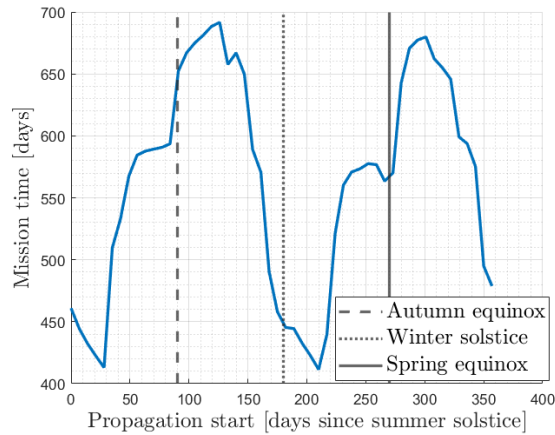
Fig. 17 Mission time as a function of the mission start date using the $A^n D$ blending method.

Figure 17 shows that the mission times resulting from starting dates between the summer solstice and the winter solstice are approximately equal to the mission times resulting from starting dates between the winter solstice and the summer solstice and therefore a periodicity is present. The spread of mission times for different starting epochs t_0 is large: the mission time has a variation of 25% depending on the initial epoch. Figure 6 shows that for a mission starting

33

time during the winter solstice, the orientation of $\vec{\lambda}_e$ with respect to $\vec{r}_{Sun-sail}$ is optimal, assuming $\Omega = \omega = i = 0$ deg, $e \ll 1$ and $e > e_{\text{target}}$.

From the visualisation of Figure 6, it is expected that starting dates near the winter solstice lead to the shortest mission times, while starting dates near the summer solstice lead to the longest mission times, explained by a difference in cone angle. However, that situation only holds for $\Omega = \omega = i = 0$ deg, $e \ll 1$. From the simulations which are performed for investigating the effect of seasonal variation on the mission time results, it is seen that both Ω and ω change significantly during the propagation. This change of orbital elements occurs in such a way that starting dates near the spring and autumn equinoxes lead to longer mission times, while starting dates near the winter and summer solstices lead to shorter mission times. Thus, the significant difference in behaviour of Ω and ω during the outward transfer for different mission start dates is the main cause for the strong seasonal variation of mission times seen in Figure 17.

B. Sail area

While the relation between the sail area and the mission time is generally well understood, it is known from literature that even for relatively simple cases such as Earth-escape trajectories with solar sailing, the curve of the time of flight as a function of the sail area or lightness number is not a smooth curve [39]. Simulations are performed to analyse the mission time behaviour for varying sail areas. Table 6 shows the simulation settings used for this test case under the name "Sail area sensitivity". The mission time results for starting times during different equinoxes and solstices are shown in Figure 18.
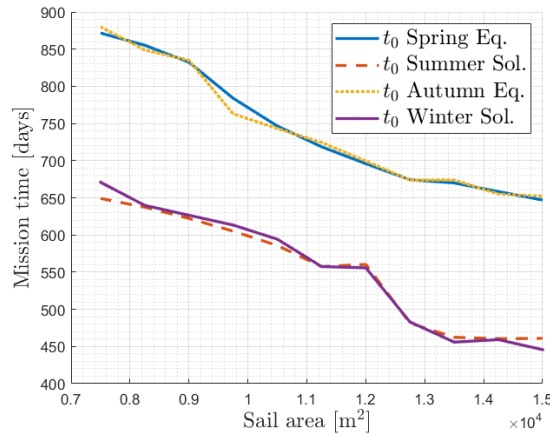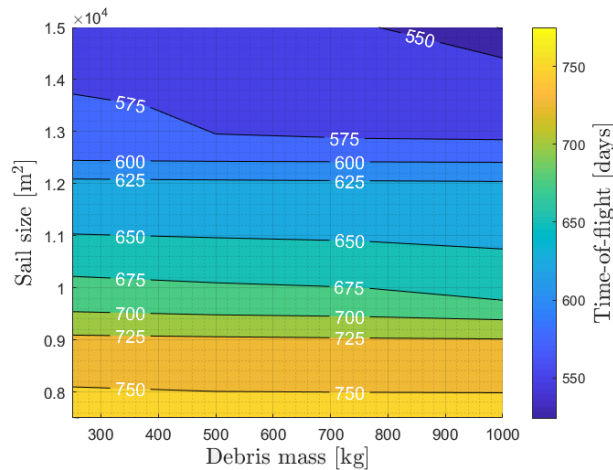

Fig. 18   Sensitivity of the mission time to the sail area using the A^nD blending control, for starting times t_0 during different solstices (sol.) and equinoxes (eq.).

Figure 18 shows that a larger sail area leads to a smaller mission time. It can be seen that the behaviour of the mission time as a function of the sail area is similar for starting times during either solstice on one side and either equinox on the other side. Further analysis shows that the relationship between the sail area and the mission time

34

does not follow an exponential trend seen in the research on Earth-escape trajectories by Macdonald [39]. The lack of exponential trend can be explained by the seasonal dependence of the orientation of $\vec{\lambda}_e$ to $\vec{r}_{Sun-sail}$, while $\vec{\lambda}_a$, used for Earth-escape strategies, does not show this seasonal dependence.

C. Debris mass

The debris mass is a relevant parameter during the outward transfer, as it influences both the lightness number and the boundary conditions for the end of the outward transfer. Therefore, a sensitivity analysis is performed for the debris object mass m_d. Simulation settings can be found in Table 6 under the name "Debris mass sensitivity". The resulting mission times for a variety of debris object masses m_d and sail areas A are shown in Figure 19. The mission time results of this graph are averaged for starting times at the summer solstice and the autumn equinox, as Figure 17 shows a dependence between the mission time and the time of the initial epoch.
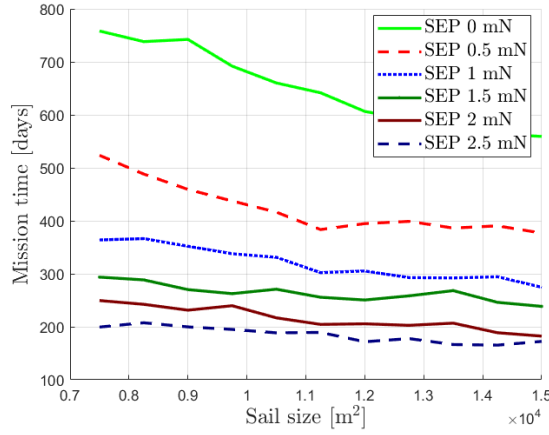

Fig. 19   Sensitivity of the mission time to the sail area and debris object mass using the A^nD blending control. Mission times are averaged for start dates at the summer solstice and the autumn equinox.

Figure 19 shows mostly horizontal lines for the mission times as a function of debris mass. Therefore, usage of the A^nD blending method for the GEO use case leads to mission times which are almost independent of the debris mass. This debris mass independence stems from the relatively short duration of the outward transfer using the A^nD blending control. The short duration of the outward transfer is not seen in other literature regarding solar-sailing applications for GEO debris removal and as such, the fact that mission times are independent of the debris object mass cannot be generalised [14, 15].

D. SEP acceleration

The mission times for a repeatable GEO debris removal mission using only SRP acceleration have been shown to be relatively large, even using the numerically optimised control of Kelly and Mei [15] [16]. The coupling of the

SRP-acceleration magnitude and direction have been shown to be impactful for the mission design for the GEO use case. In this section, a hybrid SEP/SRP-propulsion system is analysed instead and the influence of additional SEP acceleration on the mission time results is investigated. The control of the direction of SEP acceleration has been discussed in subsection IV.D. Simulations are performed for the same range of sail areas as in subsection VI.B for various SEP thrust levels and are averaged over different times for the first epoch. Simulation settings can be found in Table 6 under the name "SEP acceleration sensitivity". The mission time results are shown in Figure 20.

Fig. 20   Sensitivity of the mission time to the sail area and the SEP-thrust level using A^{n}D blending control. Mission times are averaged for different mission start dates during the year 2000.

Figure 20 shows that mission times decrease for increasing SEP thrust levels, though the difference between the mission time results using 0 mN of SEP thrust and 0.5 mN of SEP thrust is larger than the difference between, for example, the mission time results using 2 mN of thrust versus 2.5 mN of thrust, both in an absolute and in a relative sense.

One reason which has been found for this behaviour concerns the direction of $\vec{a}_{Tot} = \vec{a}_{SRP} + \vec{a}_{SEP}$. An increase in $|\vec{a}_{SEP}|$ changes both the magnitude and the direction of $\vec{a}_{Tot}$. However, the values for the SEP thrust have been chosen such that $a_{SRP} >> a_{SEP}$ for most configurations, in order to focus on the potential of solar sailing on the GEO use case, not on the potential of SEP propulsion. SEP acceleration can therefore not significantly change the direction of $\vec{a}_{Tot}$ and this can become problematic when the direction of $\vec{a}_{Tot}$ does not lead to the desired increase or decrease of an orbital element k. For these instances, it is seen that also for larger magnitudes $|\vec{a}_{SEP}|$, $\vec{a}_{Tot}$ cannot be pointed in a direction leading to the desired change of k. Despite a larger acceleration magnitude, no progress is then made to reach the target. This behaviour is illustrated by a simplified example in Figure 21, where total accelerations $\vec{a}_{Tot}$ in the red region would lead to $\frac{dk}{dt}$ having the wrong sign considering the target value and the current value of an orbital element. Using thrust levels much larger than the ones used in this work would bring the total acceleration vector $\vec{a}_{Tot}$ into the green region and the behaviour seen in Figure 20 would likely change.
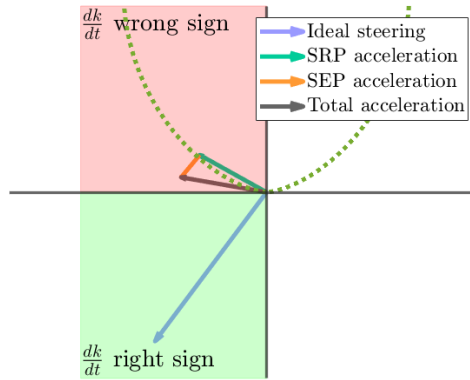
Fig. 21   Illustration how a changing magnitude of $\vec{a}_{SEP}$ does not always lead to a larger rate of change $\frac{dk}{dt}$. Simplified example.

With the addition of SEP acceleration, propellant consumption is introduced. The amount of consumed propellant has a relation with the SEP thrust via Eq. (18) and Eq. (19). The relation between the amount of consumed propellant and the mission time for various SEP-thrust levels is shown in Figure 22. Figure 22 shows a linear trend for the amount of consumed propellant as a function of the mission time with larger slopes corresponding to larger SEP thrust levels. Since the amount of consumed propellant is directly proportional to the duration of thrust and therefore the mission time, a larger amount of consumed propellant for the same thrust level is associated with a longer mission time, as a smaller sail area is used and the analysis concerns a constant maximum thrust magnitude. Mission time variation in Figure 20 is therefore a result of varying sail area only. It can also be concluded that even for the largest SEP thrust, during one round-trip mission a maximum of 1.3 kg of propellant is consumed. Therefore, only for tens of consecutive round-trip debris removal missions, the SEP-propellant consumption could become prohibitive, following the assumptions mentioned in subsection III.D.
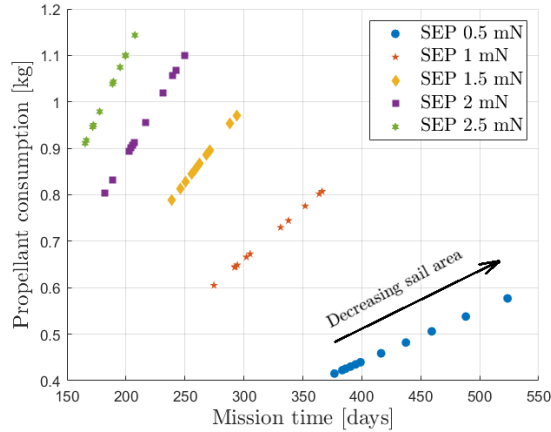
Fig. 22 The reduction in mission time compared to no usage of SEP versus the amount of consumed propellant for different SEP-thrust levels. Different points of the same colour and shape refer to results for different sail areas from Figure 20.

VII. Conclusions

In this paper, the potential of solar sailing for repeatable GEO debris removal was analysed using the accessibility-and-deficit blending ($A^n D$) method developed by Macdonald and McInnes to determine the optimal solar-sail angles that minimise the round-trip time between GEO and the graveyard orbit. The $A^n D$ blending method performed relatively well compared to other analytical control methods with a similar complexity, such as a piecewise-constant attitude approach or using the locally optimal steering law for optimally changing the pericenter. However, the $A^n D$ blending method was unable to replicate trajectory solutions like the ones obtained through numerical optimisation methods, such as particle swarm optimisation or pseudospectral control as seen in literature. The resulting trajectories from the $A^n D$ blending method resulted in round-trip mission times ranging from 630 to 760 days, which are a factor 1.4 to 5.1 larger than the results found in literature using similar simulation settings. Two reasons which were found for this discrepancy were that on average relatively large cone angles and smaller sail accelerations resulted from the $A^n D$ blending control compared to numerical control methods. Additionally, the $A^n D$ blending control resulted in large values for the semi-major axis and the eccentricity once the outward transfer was completed to satisfy the pericenter altitude constraint imposed on the graveyard orbit. Consequently, it took more time using the $A^n D$ blending control to reduce the values of these orbital parameters to return to the GEO region. Additionally, it was found that the mission times were very dependent on tuning parameters for the $A^n D$ blending method and that they were subject to seasonal variations. The results from literature showed a variation in mission times of 3% for various mission start dates, while this variation was 25% for the results from the $A^n D$ blending method. Therefore, numerical control methods perform better in terms of handling the change in dynamics throughout different seasons. It can be concluded that the usage of the $A^n D$ blending method for a preliminary mission analysis for repeatable GEO debris removal trajectories poses

38

challenges because of the inconsistency of the mission time results for different initial conditions.

It was found that mission times can be significantly reduced using an additional low-thrust propulsion system such as solar electric propulsion (SEP). It was derived that the accelerations due to solar radiation pressure and the SEP engine can be optimised independently. Using the locally optimal steering laws as a basis, the optimal SEP thrust direction was found to be equal to the direction of ideal thrust $\vec{\lambda}_k$ for changing a particular orbital element k. Mission times were reduced from a range of 560-765 days without SEP acceleration to 385-520 days with 0.5 mN of SEP thrust. This situation represents an SEP-acceleration magnitude equal to 0.5% of the characteristic acceleration of the sail.

References

[1] McInnes, C. R., *Solar sailing: technology, dynamics and mission applications*, Springer Science & Business Media, 2004.

[2] Prado, J.-Y., Perret, A., and Pignolet, G., "Using a solar sail for a plasma storm early warning system," *Environment Modeling for Space-Based Applications*, Vol. 392, 1996, p. 213. URL `https://adsabs.harvard.edu/pdf/1996ESASP.392..213P`, DoA: 2022-11-7.

[3] Forward, R. L., "Roundtrip interstellar travel using laser-pushed lightsails," *Journal of Spacecraft and Rockets*, Vol. 21, No. 2, 1984, pp. 187–195. https://doi.org/https://doi.org/10.2514/3.8632.

[4] Biesbroek, R., Aziz, S., Wolahan, A., Cipolla, S.-f., Richard-Noca, M., and Piguet, L., "The Clearspace-1 mission: ESA and Clearspace team up to remove debris," *Proc. 8th Eur. Conf. Sp. Debris*, 2021, pp. 1–3. URL https://conference.sdo.esoc.esa.int/proceedings/sdc8/paper/320/SDC8-paper320.pdf, DoA: 2022-11-7.

[5] Jones, A., "China's Shijian-21 towed dead satellite to a high graveyard orbit," *SpaceNews*, 2022. URL https://spacenews.com/chinas-shijian-21-spacecraft-docked-with-and-towed-a-dead-satellite/, DoA: 2022-11-7.

[6] Valk, S., Lemaître, A., and Deleflie, F., "Semi-analytical theory of mean orbital motion for geosynchronous space debris under gravitational influence," *Advances in Space Research*, Vol. 43, No. 7, 2009, pp. 1070–1082. https://doi.org/https://doi.org/10.1016/j.asr.2008.12.015.

[7] Yakovlev, M., "The "IADC Space Debris Mitigation Guidelines" and supporting documents," *4th European Conference on Space Debris*, Vol. 587, ESA Publications Division Noordwijk, The Netherlands, 2005, pp. 591–597. URL https://conference.sdo.esoc.esa.int/proceedings/sdc4/paper/35/SDC4-paper35.pdf, DoA: 2022-11-7.

[8] Lála, P., "Space Debris Issue at the United Nations," *Annals of the New York Academy of Sciences*, Vol. 822, No. 1, 1997, pp. 611–620. URL https://link.springer.com/article/10.1023/A:1021231027859, DoA: 2022-11-7.

[9] Kuznetsova, O., and Rozentsvaig, A., "International legal problems of the ecology of outer space," *International Youth Scientific Conference "XV Royal Readings"*, 2019, pp. 999–1000. URL http://repo.ssau.ru/handle/Mezhdunarodnaya-molodezhnaya-nauchnaya-konferenciya-Korolevskie-chteniya/International-legal-problems-of-the-ecology-of-outer-space-80215, DoA: 2022-11-7.

[10] Cunio, P. M., Bantel, M., Flewelling, B. R., Therien, W., Jeffries Jr, M. W., Montoya, M., Butler, R., and Hendrix, D., "Photometric and other analyses of energetic events related to 2017 GEO RSO anomalies," *Proceedings of the Advanced Maui Optical and Space Surveillance (AMOS) Technologies Conference*, 2017. URL https://amostech.com/TechnicalPapers/2017/Poster/Cunio.pdf, DoA: 2022-11-7.

[11] Ludfy, A., and Rahadian, D., "Investor reaction to anomaly & recovery service of TELKOM-1 satellite year 2017," *Proceeding of International Seminar & Conference on Learning Organization*, 2018. https://doi.org/https://openlibrarypublications. telkomuniversity.ac.id/index.php/isclo/article/view/7014.

[12] Colombo, C., De Fer, T. D. B., Bewick, C., and McInnes, C., "Assessment of passive and active solar sailing strategies for end of life re-entry," Vol. 4, 2016. URL https://indico.esa.int/event/128/attachments/735/875/05_presentation_CleanSpace_Colombo.pdf, DoA: 2022-11-7.

[13] Colombo, C., Miguel Banos, N., and Gkolias, I., "Modulating solar sail control for end-of-life disposal with solar sails," 2019, pp. 1–13. URL https://re.public.polimi.it/retrieve/handle/11311/1123523/474053/COLOC08-19.pdf, DoA: 2022-11-7.

[14] Kelly, P. W., Bevilacqua, R., Mazal, L., and Erwin, R. S., "TugSat: removing space debris from geostationary orbits using solar sails," *Journal of Spacecraft and Rockets*, Vol. 55, No. 2, 2018, pp. 437–450. https://doi.org/https://doi.org/10.2514/1.A33872.

[15] Kelly, P., and Bevilacqua, R., "Geostationary debris mitigation using minimum time solar sail trajectories with eclipse constraints," *Optimal Control Applications and Methods*, Vol. 42, No. 1, 2021, pp. 279–304. https://doi.org/https://doi.org/10.1002/oca.2676.

[16] Mei, H., Damaren, C. J., and Zhan, X., "Feedback Pseudospectral Method for End-of-Life Geostationary Satellites Removal Using Solar Sailing," *Journal of Guidance, Control, and Dynamics*, Vol. 45, No. 3, 2022, pp. 570–579. https://doi.org/https://doi.org/10.2514/1.G005631.

[17] Macdonald, M., and McInnes, C. R., "Analytical control laws for planet-centered solar sailing," *Journal of Guidance, Control, and Dynamics*, Vol. 28, No. 5, 2005, pp. 1038–1048. https://doi.org/https://doi.org/10.2514/1.11400.

[18] Chernyakina, I. V., "Solar sailing in realistic mode, based on a locally-optimal control laws," *Advances in Space Research*, Vol. 67, No. 9, 2021, pp. 2844–2854. URL https://doi.org/10.1016/j.asr.2020.01.032, DoA: 2022-11-7.

[19] Shi, X., Guo, J., Cui, N., and Huang, R., "Blending optimal algorithm for heliocentric solar sailing," *Aircraft Engineering and Aerospace Technology*, 2013. URL https://doi.org/10.1108/00022661311302751, DoA: 2022-11-7.

[20] Niccolai, L., Quarta, A. A., and Mengali, G., "Analytical solution of the optimal steering law for non-ideal solar sail," *Aerospace Science and Technology*, Vol. 62, 2017, pp. 11–18. https://doi.org/https://doi.org/10.1016/j.ast.2016.11.031.

[21] ESA space debris office, "ESA's Annual Space Environment Report," , 2020. URL https://www.sdo.esoc.esa.int/environment_ report/Space_Environment_Report_latest.pdf, DoA: 2022-11-7.

[22] ESOC, "Space Environment Statistics - Environment Report," , 2020. URL https://sdup.esoc.esa.int/discosweb/statistics/, DoA: 2022-11-7.

[23] Chebotarev, V., and Vnukov, A., "Cost Efficiency Analysis of Space Debris Removal from Geostationary Orbit Using Service Spacecraft," 2018. https://doi.org/https://doi.org/10.2991/avent-18.2018.14.

[24] Badhwar, G. D., "Determination of the area and mass distribution of orbital debris fragments," *Earth, Moon, and Planets*, Vol. 45, No. 1, 1989, pp. 29–51. https://doi.org/https://doi.org/10.1007/BF00054659.

[25] de Veld, F., "Solar sailing for active space debris removal: GEO debris removal with hybrid low-thrust propulsion," , Literature Study, Delft University of Technology, 2021.

[26] Valk, S., Delsate, N., Lemaître, A., and Carletti, T., "Global dynamics of high area-to-mass ratios GEO space debris by means of the MEGNO indicator," *Advances in Space Research*, Vol. 43, No. 10, 2009, pp. 1509–1526. https://doi.org/https://doi.org/10.1016/j.asr.2009.02.014.

[27] Spencer, D. A., Johnson, L., and Long, A. C., "Solar sailing technology challenges," *Aerospace Science and Technology*, Vol. 93, 2019, p. 105276. https://doi.org/https://doi.org/10.1016/j.ast.2019.07.009.

[28] Clark, S., and Randall, P. e. a., "BepiColombo—Solar Electric Propulsion System Test and Qualification Approach," 2019. URL http://electricrocket.org/2019/586.pdf, DoA: 2022-11-7.

[29] Hintz, G. R., "Survey of orbit element sets," *Journal of guidance, control, and dynamics*, Vol. 31, No. 3, 2008, pp. 785–790. https://doi.org/https://doi.org/10.2514/1.32237.

[30] Montenbruck, O., Gill, E., and Lutze, F., "Satellite orbits: models, methods, and applications," *Appl. Mech. Rev.*, Vol. 55, No. 2, 2002, pp. B27–B28.

[31] Wakker, K., *Fundamentals of Astrodynamics*, Institutional Repository Library, Delft University of Technology, 2015.

[32] Heiligers, J., Fernandez, J. M., Stohlman, O. R., and Wilkie, W. K., "Trajectory design for a solar-sail mission to asteroid 2016 HO3," *Astrodynamics*, Vol. 3, No. 3, 2019, pp. 231–246. https://doi.org/https://doi.org/10.1007/s42064-019-0061-1.

[33] Carzana, L., Visser, P., and Heiligers, J., "Locally optimal control laws for Earth-bound solar sailing with atmospheric drag," *Aerospace Science and Technology*, 2022, p. 107666. https://doi.org/https://doi.org/10.1016/j.ast.2022.107666.

[34] Kéchichian, J. A., "Inclusion of higher order harmonics in the modeling of optimal low-thrust orbit transfer," *The Journal of the Astronautical Sciences*, Vol. 56, No. 1, 2008, pp. 41–70. https://doi.org/https://doi.org/10.1007/BF03256541.

[35] Heiligers, J., McInnes, C. R., Biggs, J. D., and Ceriotti, M., "Displaced geostationary orbits using hybrid low-thrust propulsion," *Acta Astronautica*, Vol. 71, 2012, pp. 51–67. https://doi.org/https://doi.org/10.1016/j.actaastro.2011.08.012.

[36] Williams, D., "Moon Fact Sheet," , 2021. URL https://nssdc.gsfc.nasa.gov/planetary/factsheet/moonfact.html, DoA: 2022-11-7.

[37] Williams, D., "Sun Fact Sheet," , 2021. URL https://nssdc.gsfc.nasa.gov/planetary/factsheet/sunfact.html, DoA: 2022-11-7.

[38] Roy, A. E., *Orbital motion*, CRC Press, 2004.

[39] Macdonald, M., and McInnes, C. R., "Realistic earth escape strategies for solar sailing," *Journal of Guidance, Control, and Dynamics*, Vol. 28, No. 2, 2005, pp. 315–323. https://doi.org/https://doi.org/10.2514/1.5165.

3

Conclusions and recommendations

The aim of this work was to assess different analytical control methods for solar sailing regarding the use case of repeated geostationary debris removal, with a focus on the accessibility-and-deficit blending method developed by Macdonald and McInnes [15]. With a well-performing analytical method resulting in reliable mission times, a wide parameter space can be analysed in terms of their resulting mission times in a much shorter time span than with computationally intensive numerical control methods, based on numerical optimisation methods. Assessment was performed mostly on mission times, but also on the behaviour of control variables and relevant orbital parameters. A secondary aim of this work was to investigate the influence of the additional usage of a solar electric propulsion (SEP) engine on the results. The conclusions of this work are described in Section 3.1 and the recommendations for further research in Section 3.2.

3.1. Conclusions

Section 1.2 presented six research questions: one regarding the comparison between analytical and numerical control laws, two regarding the resulting mission times and mission time dependencies, two about the influence of the addition of SEP acceleration, and one general research question about solar sailing. Beneath, they are answered individually.

- **Do analytical control methods for solar sailing form a usable alternative to numerical control methods for trajectory planning for one cycle from GEO to the graveyard orbit and back?**
  The trajectories from GEO to the graveyard orbit and back resulting from the usage of analytical control methods, in particular the A^nD blending method, have significantly longer mission times than their counterparts originating from numerical control, using the same initial parameters. A comparison between the results from this thesis and results from literature is shown in Table 3.1, where 'out' refers to the outward transfer from GEO to the graveyard orbit, and 'in' to the inward transfer from the graveyard orbit to GEO. Looking at the results from Kelly (2017), who used Lyapunov control to simulate a solar-sail assisted return mission from GEO to the graveyard orbit, resulted in a mission time of 450 days for numerical control and 630 days for analytical control. This difference between analytical and numerical control is even larger with the results from Kelly (2021), who used a Gaussian quadrature implicit integration method for optimisation of the control. The A^nD blending method resulted in a mission time of 759 days, compared to 150 days from numerical control. Lastly, comparison with the mission time of Mei (2022), who used pseudospectral control, resulted in a mission time of 625 days with analytical control and 350 days using numerical control.

  While the mission times are larger using A^nD blending control, the A^nD blending method results in valid trajectories which can be followed by a spacecraft. During these trajectories, the cone and clock angles are relatively large compared to values from literature. The debris removal trajectories resulting from the analytical control method do not appear to have benefits over the trajectories from literature, obtained through numerical optimisation.

  The A^nD blending method could potentially be used for parameter space reduction for preliminary mission analysis, in the sense that the mission time for a set of parameters could roughly be estimated before a full control optimisation takes place. Based on the resulting mission time, a decision can be made whether numerical optimisation would yield interesting results. Two main issues persist prohibiting the usage of the A^nD blending method for preliminary mission analysis. Firstly, the trajectories resulting from the A^nD blending control are dependent on the mission start date and seasonal variation throughout the trajectory in a complex way, leading to variations in the resulting mission time up to 25% for equal mission parameters. In literature, the variation in mission times for different mission start dates is found to be only 3% [20]. Mission

time results using A^{n}D blending control are therefore difficult to generalise, even more so than for mission time results using numerical control methods. Secondly, only three test cases from literature could be used for validation during this thesis, which all make use of different numerical control methods, and these test cases do not provide mission time results for a variety of mission parameters. The lack of results for comparison made it impossible to understand whether analytical control methods can be successfully used for preliminary mission time analysis. Additionally, the mission parameters of two test cases from literature were not realistic, except for the results from Mei (2022). This realism mostly refers to the sailcraft mass, which is much smaller in the work of Kelly (2017) and Kelly (2021) than what is currently feasible. A wider catalogue of mission time results using numerical control methods for realistic mission parameters is needed to make a complete comparison between numerical and analytical control methods for the GEO use case.

Table 3.1: Results from literature compared with results from the A^{n}D blending method [20]–[22]. A/M-ratio: Area-to-mass ratio, reprod.: reproduction

Parameter	Kelly (2017)	Reprod.	Kelly (2021)	Reprod.	Mei (2022)	Reprod.
A/M-ratio (out) [m^2 kg^{-1}]	0.76	0.76	1	1	0.14	0.14
A/M-ratio (in) [m^2 kg^{-1}]	16	16	12	12	-	-
Transfer time (out) [days]	220	165	90	119	350	625
Transfer time (in) [days]	250	465	60	640	-	-
Transfer time (tot) [days]	450	630	150	759	350	625
Factor difference w. literature	-	1.4	-	5.1	-	1.8

- **2. What is the minimal time required for re-orbiting geosynchronous debris to the graveyard orbit and manoeuvring back to GEO using solar sailing as the only form of propulsion?**
  Table 3.1 shows the mission time results for various area-to-mass ratios for the outward and inward transfers, with the round-trip mission time varying between 630 days and 760 days. However, from the results of this work and the comparison with values from literature, it can be concluded that analytical control methods based on locally optimal steering laws do not result in truly minimal time trajectories, and the mission times of the trajectories originating from analytical control methods can be much reduced using numerical control methods. Thus, minimum times for the GEO use case are still only found in literature. The fact that analytical control methods do not lead to minimum-time trajectories can be explained based on the relatively simple control compared to complex numerical optimisation. Contrary to mission cases like Earth-escape trajectories, the mission case of GEO debris removal has proven to be too complex for analytical control to match the results of numerical control. The A^{n}D blending method, even when calibrated for the GEO use case, is not able to limit the increase in semi-major axis and eccentricity to satisfy the pericenter altitude constraint imposed on the graveyard orbit to the same extent that numerical control methods do. It takes much time to decrease these relatively large values for the semi-major axis and eccentricity again to return to GEO.

- **2a. How do parameters like mission start date, solar-sail area, debris mass and debris orbital parameters influence the mission time results?**
  Seasonal variation has been shown to be influential for the mission time results. The orientation of the locally optimal steering direction for the eccentricity compared to the Sun-sail line varies significantly during one year, which results in large variations of the cone and clock angle. It was seen that a different starting epoch t_0 can either increase or decrease the mission time by 25%. The influence of the seasonal variation on the mission time is difficult to predict, since the longitude of the ascending node Ω and the argument of periapsis ω vary considerably throughout the trajectory.

  The relation between the mission time and the solar-sail area was found to resemble an exponential relationship, though the seasonal variation throughout the trajectory creates a deviation from this type of relation. Averaged for different initial epochs t_0, the mission time was 560 days for a sail area of 15000 m^2, a solar-sail satellite mass of 500 kg and a debris mass of 500 kg, while it was 765 days for the same situation with a sail area of 7500 m^2.

  The dependence of the mission time on the debris mass was almost none. Differences between simulations with different debris masses are caused by seasonal variation. The expectation was a slight decrease in mission time for constant sail area and larger debris masses, since the graveyard orbit is defined based on a pericenter requirement. A larger debris object mass leads to a smaller required pericenter value for releasing the debris object, after which the sailcraft returns to GEO. However, the main reason why the debris mass has little influence on the mission time results is because the mission segment before releasing the debris object, when the debris object mass has an influence on the lightness number, is much shorter than the mission segment after the release, using A^{n}D blending control as the control method. This same mission

profile was not seen in literature and thus the result that the debris object mass has no influence on the mission time cannot be automatically extrapolated.

Lastly, the dependence on the target orbital elements for the inward transfer was found to be significant. The eccentricity target value was found to be the most influential, as orbit circularisation took more time than semi-major axis reduction. A target eccentricity of 0.005 instead of 0.0005 can reduce the mission time by 30%. However, most debris objects in GEO have orbits with eccentricities in the order of 0.0005 or smaller. The mission time difference in targeting an eccentricity of 0.0005 and smaller eccentricities is very minor. Therefore, the variation in target orbital elements for GEO debris objects for realistic cases has little influence on the mission time.

- **2b How does additional usage of an SEP-engine influence the mission time results?**
  It was found that usage of SEP thrust has a significant effect on the mission time. For a sail area of 7500 m^2, a debris mass of 500 kg and a sailcraft mass of 500 kg, an SEP thrust of 0.5 mN decreased the mission time from 765 with no usage of an SEP engine to 520 days, while the solar-sail characteristic acceleration is 200 times larger than the acceleration provided by the SEP engine. The cone angle of the sail is relatively large throughout most of the trajectories following the A^{n}D blending control, averaging over 60 deg. This means that the SRP acceleration for most of the trajectories is only a small fraction of the characteristic acceleration. Since the magnitude of SEP acceleration is not dependent on its direction, the SEP engine can directly thrust in the ideal direction of thrust, which greatly reduces the mission time. Relatively large cone angles throughout the trajectory were also seen in literature, though still much smaller than the cone angles found in this thesis, giving an indication that for numerical control too, the addition of an SEP engine would be very influential on the mission time results.

- **3. Is it possible to explain the influence of SEP-thrust on the minimal-time results analytically?**
  Like the relationship between the mission time and the sail area without SEP acceleration, the relationship between the mission time and the sail area with SEP acceleration resembles an exponential relationship. However, different SEP accelerations result in different trends. The reduction in the mission time is not constant for a constant increase in SEP acceleration. A reason for this discrepancy is the direction of the SRP acceleration $\vec{a}_{SRP}$. If the cone angle α is small and the inner product of $\vec{a}_{SRP}$ and the ideal direction of thrust $\vec{\lambda}_k$ is large, $\vec{a}_{SRP}$ is a beneficial direction of thrust, since this direction leads to the desired increase or decrease of an orbital element k. However, when α is large, $\vec{a}_{SRP}$ is not necessarily a beneficial direction of thrust, and for periods during the trajectory, the total acceleration does not lead to the desired increase or decrease of an orbital element. For these short periods during the trajectory, the total acceleration magnitude is then still larger compared to the case without SEP acceleration, but the SEP acceleration does not lead aid in changing the orbital elements. Overall, the SEP acceleration still leads to a decrease in mission time however.

- **4. Does solar sailing form an advantageous form of propulsion for GEO debris removal compared to existing propulsion methods?**
  This question cannot be fully answered following the results of this work, but some important notions were gained. Firstly, the nature of the GEO use case leads both in this work and in existing literature to remarkably large cone angles and thus small sail accelerations. This is an indication that the GEO use case is not ideal for solar sailing. However, in recent years, significant advancements have been made in decreasing theoretical mission times in the GEO use case with solar sailing, leading to mission times with realistic solar-sailing parameters in the order of a few years. It has not been explicitly shown that unfavourable dynamics are the direct cause of a large average cone angle throughout the trajectory. Advancements in the state-of-the-art of optimisation algorithms for solar-sailing could lead to different trajectories with much smaller average cone angles, which would make solar sailing for GEO debris removal an attractive option. Therefore, small sail accelerations are not necessarily prohibitive for applying solar sailing for geostationary debris removal. However, the main advantage of solar sailing is its potential for repeatable debris removal. While this concept has not been investigated much in this thesis, a subsequent debris removal mission has minimal relation with the previous mission part. The only connection is that the end and start orbital parameters must match. Therefore, solar sailing is an attractive method of propulsion in terms of sustainability and re-usability. For existing methods of propulsion, during each round-trip mission additional fuel is consumed. It was found that for the largest thrust values used in this thesis, 1.3 kg of propellant is consumed. More research is needed to assess what propulsion method is more advantageous for repeatable GEO debris removal: solar sailing, SEP or a hybrid.

3.2. Recommendations

Since the research of this thesis is in the relatively new area of active space debris removal using solar sails, much research is still left to explore, and this thesis has resulted in several recommendations for further research. If followed, these can lead to mission time results which are more generally applicable and reliable. More insight can be given into truly minimum-time trajectories, since the trajectories found in this research have been the result of analytical control rather than numerical control using optimisation algorithms. The recommendations are given in several categories, namely satellite control, mission context and dynamics.

3.2.1. Sailcraft control

The main recommendation regarding the satellite control is to perform numerical optimisation to find minimum-time trajectories for a range of mission parameters, instead of using analytical control, as it was seen that the results coming from numerically optimised control resulted in much smaller mission times than the ones found in this thesis based on analytically derived control. The optimised mission times for the GEO use case using the analytical optimisation methods of this thesis do not match the optimised mission times using numerical control from literature. It would be interesting to apply global optimisation methods to this GEO use case, contrary to local optimisation methods which are used in this thesis. Especially when the trajectories themselves become more complex, for example through the addition of more constraints, numerical optimisation is crucial to obtain minimum-time trajectories. Once a wider variety of mission parameters and the corresponding optimised trajectories is obtained, a better understanding of the relationship between the results coming from numerical control methods and analytical control methods can also be obtained. With this, the usefulness of analytical control methods for preliminary parameter search can be investigated, as this is not fully possible using current literature.

SEP acceleration throttling

In this research, only two advantages of the addition of SEP acceleration have been investigated, namely the ability to thrust in an arbitrary direction and the extra acceleration that SEP provides. One other important advantage is the possibility to control the SEP-acceleration magnitude independently of the SEP-acceleration direction, which is impossible with SRP acceleration only. Since the total acceleration along an optimal thrust direction $\vec{\lambda}$ was always maximised during this research, purposely decreasing the SEP acceleration magnitude was never relevant. For more realistic mission analyses, throttling the SEP thrust is expected to be advantageous when preventing overshooting and reducing propellant consumption.

3.2.2. Mission context

In practice, a significant part of a GEO debris removal mission would consist of rendezvous and capture of the debris object. While this concept has been studied for some use cases, this has never been studied in the context of solar sailing, and little in the context of GEO debris removal [23]. During this thesis, phasing, rendezvous and capture has not been considered because of the additional complexity this yields. It is recommended to study these steps in detail in the context of solar sailing.

Something which did not come up during this thesis is the targeting of specific debris objects, rather than only the semi-major axis and eccentricity of their orbit. Preliminary work was performed by Kelly and Bevilacqua, but only for one hypothetical object [20]. Targeting debris objects with known ephemerides data and analysing which debris objects pose the most risk to satellites would be an important step towards realising a solar-sailing debris removal mission.

3.2.3. Dynamics

Significant improvements in the accuracy of the results can be obtained through increasing the fidelity of the dynamical model and the accuracy of the integrator. This thesis used an ideal solar-sail model, although optical sail models or more advanced models are more realistic. Using a more realistic sail model, as well as implementing additional features such as temperature-dependent solar-sail accelerations and technical constraints for cone and clock angles, can influence the results for variables such as mission time by up to 15% [24].

Assumptions were also made regarding the dynamical model. High-fidelity dynamical models, including for example the Earth spherical harmonics coefficients up to degree and order four and the implementation of a more advanced eclipse model than the currently used discontinuous eclipse model, can become a useful addition to the simulation environment. It is important to note that these additions are only a useful addition when assumptions leading to larger errors in the results have been accounted for, such as the choice of the solar-sail model.

An interesting idea which could reduce the computational time is to use the Earth-Centred, Earth-Fixed reference frame ($\mathcal{E}_{ECEF}$) for propagation instead of the $\mathcal{E}_{ECI}$ reference frame. The $\mathcal{E}_{ECEF}$ frame is a co-rotating reference frame with the rotation rate equal to the one of the Earth. The rotation rate of the Earth is not necessarily relevant to this research work, but trajectories from GEO to the graveyard orbit would be much less complex than in the $\mathcal{E}_{ECI}$ reference frame. In the $\mathcal{E}_{ECEF}$ frame, the trajectory for a total round-trip mission would only likely cover

a fraction of a revolution in this frame, compared to hundreds of revolutions in the $\mathcal{E}_{ECI}$ reference frame. Possibly, defining the problem in the $\mathcal{E}_{ECEF}$ reference frame could then reduce the computational load of performing propagations. In literature, the $\mathcal{E}_{ECEF}$ frame is seen in the work of Kelly (2021) [20].

Bibliography

[1] L. Casson, *Ships and seamanship in the ancient world*. JHU Press, 1995.

[2] J. C. Maxwell, *A dynamical theory of the electromagnetic field*. Wipf and Stock Publishers, 1996.

[3] J. Verne, *De la terre à la lune: trajet direct en 97 heures 20 minutes*. Bibliotheque d'Education et de Récréation, 1866.

[4] D. A. Spencer, L. Johnson, and A. C. Long, "Solar sailing technology challenges", *Aerospace Science and Technology*, vol. 93, p. 105 276, 2019. DOI: https://doi.org/10.1016/j.ast.2019.07.009.

[5] M. Urbanczyk, "Solar sails-a realistic propulsion for spacecraft", Tech. Rep., 1967.

[6] L. McNutt, L. Johnson, P. Kahn, J. Castillo-Rogez, and A. Frick, "Near-earth asteroid (nea) scout", in *AIAA Space 2014 Conference and Exposition*, 2014, p. 4435. DOI: https://doi.org/10.2514/6.2014-4435.

[7] J.-Y. Prado, A. Perret, and G. Pignolet, "Using a solar sail for a plasma storm early warning system", in *Environment Modeling for Space-Based Applications*, DoA: 2022-11-7, vol. 392, 1996, p. 213. [Online]. Available: https://adsabs.harvard.edu/pdf/1996ESASP.392..213P.

[8] M. Macdonald, G. W. Hughes, C. R. McInnes, A. Lyngvi, P. Falkner, and A. Atzei, "Solar polar orbiter: A solar sail technology reference study", *Journal of Spacecraft and Rockets*, vol. 43, no. 5, pp. 960–972, 2006. DOI: https://doi.org/10.2514/1.16408.

[9] R. L. Forward, "Roundtrip interstellar travel using laser-pushed lightsails", *Journal of Spacecraft and Rockets*, vol. 21, no. 2, pp. 187–195, 1984. DOI: https://doi.org/10.2514/3.8632.

[10] ESOC, *Space environment statistics - environment report*, DoA: 2022-11-7, 2020. [Online]. Available: https://sdup.esoc.esa.int/discosweb/statistics/.

[11] D. J. Kessler, N. L. Johnson, J. Liou, and M. Matney, "The kessler syndrome: Implications to future space operations", *Advances in the Astronautical Sciences*, vol. 137, no. 8, p. 2010, 2010, DoA: 2022-11-7. [Online]. Available: https://threecountrytrustedbroker.com/media/kesseler_syndrome.pdf.

[12] L. de Gouyon Matignon, *Orbital slots and space congestion*, DoA: 2022-11-7, 2019. [Online]. Available: https://www.spacelegalissues.com/orbital-slots-and-space-congestion/.

[13] R. Biesbroek, S. Aziz, A. Wolahan, S.-f. Cipolla, M. Richard-Noca, and L. Piguet, "The clearspace-1 mission: Esa and clearspace team up to remove debris", in *Proc. 8th Eur. Conf. Sp. Debris*, DoA: 2022-11-7, 2021, pp. 1–3. [Online]. Available: https://conference.sdo.esoc.esa.int/proceedings/sdc8/paper/320/SDC8-paper320.pdf.

[14] C. R. McInnes, *Solar sailing: technology, dynamics and mission applications*. Springer Science & Business Media, 2004.

[15] M. Macdonald and C. R. McInnes, "Analytical control laws for planet-centered solar sailing", *Journal of Guidance, Control, and Dynamics*, vol. 28, no. 5, pp. 1038–1048, 2005. DOI: https://doi.org/10.2514/1.11400.

[16] M. Macdonald and C. R. McInnes, "Realistic earth escape strategies for solar sailing", *Journal of Guidance, Control, and Dynamics*, vol. 28, no. 2, pp. 315–323, 2005.

[17] G. Leemans, L. Carzana, and J. Heiligers, "Many-revolution earth-centred solar-sail trajectory optimisation using differential dynamic programming", in *AIAA SCITECH 2022 Forum*, 2022, p. 1776. DOI: https://doi.org/10.2514/6.2022-1776.

[18] H. Mei, C. J. Damaren, and X. Zhan, "Hybrid removal of end-of-life geosynchronous satellites using solar radiation pressure and impulsive thrusts", *Advances in Space Research*, vol. 66, no. 4, pp. 974–991, 2020. DOI: https://doi.org/10.1016/j.asr.2020.04.052.

[19] J. Heiligers, M. Ceriotti, C. R. McInnes, and J. D. Biggs, "Displaced geostationary orbit design using hybrid sail propulsion", *Journal of Guidance, Control, and Dynamics*, vol. 34, no. 6, pp. 1852–1866, 2011. DOI: https://doi.org/10.2514/1.53807.

[20] P. Kelly and R. Bevilacqua, "Geostationary debris mitigation using minimum time solar sail trajectories with eclipse constraints", *Optimal Control Applications and Methods*, vol. 42, no. 1, pp. 279–304, 2021. DOI: https://doi.org/10.1002/oca.2676.

[21] P. W. Kelly, R. Bevilacqua, L. Mazal, and R. S. Erwin, "Tugsat: Removing space debris from geostationary orbits using solar sails", *Journal of Spacecraft and Rockets*, vol. 55, no. 2, pp. 437–450, 2018. DOI: https://doi.org/10.2514/1.A33872.

[22] H. Mei, C. J. Damaren, and X. Zhan, "Feedback pseudospectral method for end-of-life geostationary satellites removal using solar sailing", *Journal of Guidance, Control, and Dynamics*, vol. 45, no. 3, pp. 570–579, 2022. DOI: https://doi.org/10.2514/1.G005631.

[23] F. de Veld, *Solar sailing for active space debris removal: Geo debris removal with hybrid low-thrust propulsion*, 2021.

[24] H. Spencer and K. A. Carroll, "Real solar sails are not ideal, and yes it matters", pp. 921–940, 2014, DoA: 2022-11-7. [Online]. Available: https://link.springer.com/chapter/10.1007/978-3-642-34907-2_55.

[25] A. Caruso, L. Niccolai, A. A. Quarta, and G. Mengali, "Effects of attitude constraints on solar sail optimal interplanetary trajectories", *Acta Astronautica*, vol. 177, pp. 39–47, 2020. DOI: https://doi.org/10.1016/j.actaastro.2020.07.010.

[26] C. R. McInnes, "Artificial lagrange points for a partially reflecting flat solar sail", *Journal of guidance, control, and dynamics*, vol. 22, no. 1, pp. 185–187, 1999. DOI: https://doi.org/10.2514/2.7627.

[27] K. Wakker, *Fundamentals of Astrodynamics*. Institutional Repository Library, Delft University of Technology, 2015.

[28] C. H. Acton, "Nasa's spice system models the solar system", in *International Astronomical Union Colloquium*, Cambridge University Press, vol. 165, 1997, pp. 257–262.

A
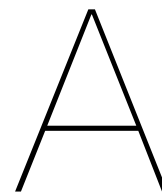
Appendix Verification and Validation

This appendix shows the various analyses performed regarding the verification of the implemented simulation environment of the thesis and the validation of the generated results, though most of the validation is performed in the journal article in the thesis through comparison with literature. The dynamical model is verified in Section A.1, the analytical control laws in Section A.2 and the implementation of SEP acceleration in Section A.3.

A.1. Dynamical model

The dynamical model of this work has been implemented completely by the author, and as such the individual parts of the dynamical model require verification. First, the acceleration verification is discussed in Subsection A.1.1 and afterwards the integration and propagation is discussed in Subsection A.1.2.

A.1.1. Accelerations

Solar-sail acceleration

Since this thesis work is based on solar sailing, a different solar radiation pressure model is used than in most literature not related to solar sailing, where cannon-ball radiation pressure models are commonplace. These solar-sail dynamics must be verified independently of other accelerations. The unique contour shape of the solar radiation pressure acceleration magnitude depending on the direction is one characteristic which can be verified, as well as characteristics as the optimised cone angle for certain ideal directions $\vec{\lambda}$. The results of this verification are shown in Figure A.1, using information from literature from Caruso et al. [25]. As can be seen, the shapes match perfectly, and the cone angle that maximises the traverse acceleration was found to be $\alpha = 35.26°$, matching the value from literature [26].

Perturbing accelerations

For the perturbing accelerations, a comparison between the acceleration values and orders of magnitude resulting from the simulation environment and the ones from Wakker is made [27], specifically for geostationary altitude. In Table A.1, the comparison is shown between values obtained from simulations and values from literature.

Table A.1: Comparison between literature and simulation values for acceleration magnitudes. PMG: Point-mass gravity, E: Earth, TBD: Third-body dynamics. M: Moon, S: Sun

| Acceleration	Magnitude, sim [m s^{-2}]	Magnitude, lit [m s^{-2}]
PMG, E	$3.1 \cdot 10^{-1}$	$3 \cdot 10^{-1}$
J2, E	$8.3 \cdot 10^{-6}$	$8 \cdot 10^{-6}$
TBD, M	$3.7 - 12.1 \cdot 10^{-6}$	$8 \cdot 10^{-6}$
TBD, S	$4.8 - 7.3 \cdot 10^{-6}$	$6 \cdot 10^{-6}$

The variation seen in the values obtained through simulation of Table A.1, especially for the third-body-perturbation of the Moon, are caused by the fact that the distance between the Moon and the satellite varies considerably during the simulation. Despite the fact that no exact comparison can be made between literature and simulation, the behaviour, order of magnitude, and direction of the simulated accelerations all match expectations, validating the implementation of SRP acceleration.

(a) SRP-acceleration contour from literature, obtained from [25].

(b) Reproduced SRP-acceleration contour from simulations
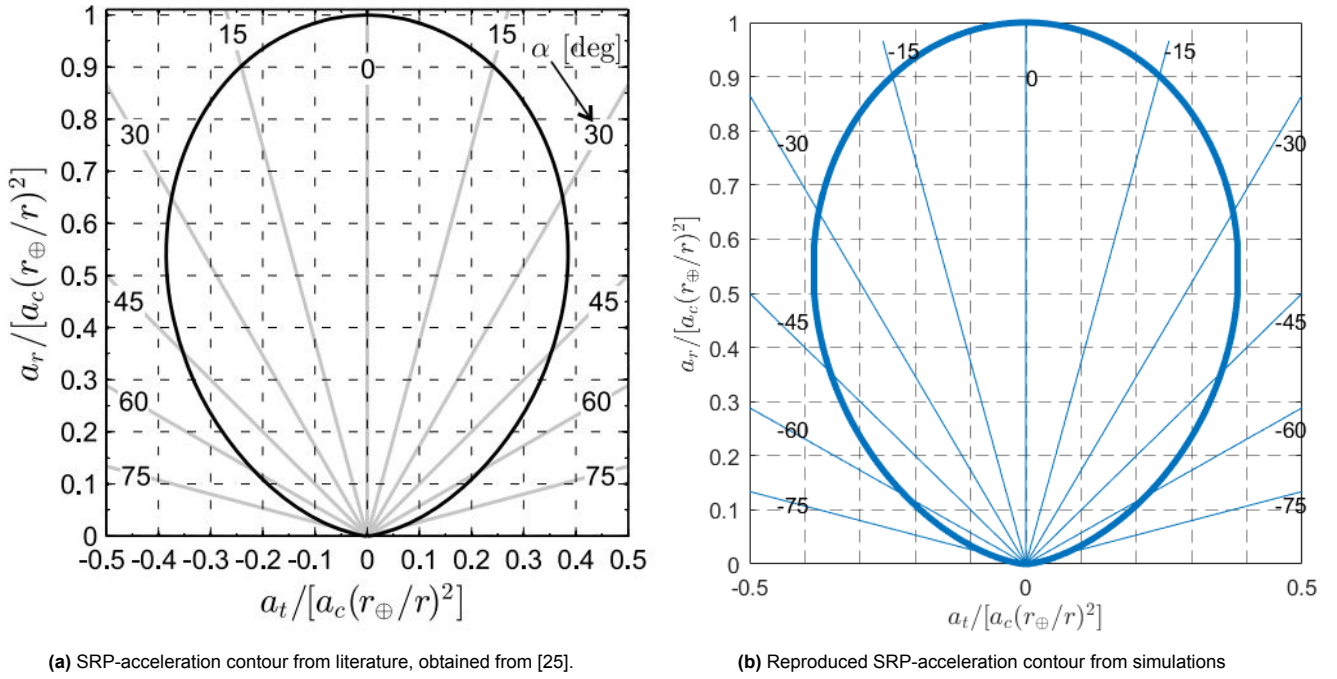
Figure A.1: Comparison between reproduced and literature values for SRP acceleration

Eclipsing

The eclipse model used in this work is rudimentary. In this model, a configuration is considered to include an eclipse if the distance of the Earth or Moon to the Sun-sail line segment is smaller than their respective radius. In Figure A.2, verification for the implementation of eclipses is shown for two elementary fictional cases where the Sun is in-plane with the Earth and the sail, where a lightness number of 0.01 is used, a constant cone angle of 45 deg and a constant clock angle of 90 deg. If the Sun is not in or very near to this plane, eclipses at GEO altitude are not possible.
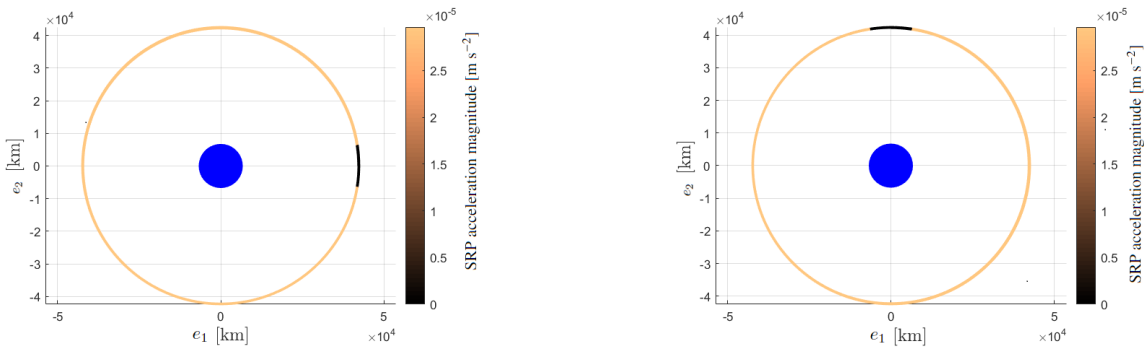
Figure A.2: Eclipse implementation verification with the Sun on the negative e_1-axis (left) and the negative e_2-axis (right)

As can be seen from the colour bar, for one segment of the trajectory, the SRP acceleration is zero. The variation in SRP acceleration along the orbit apart from eclipses is negligible for a constant cone angle, set to 45 deg in this test case. Therefore, Figure A.2 shows a correct behaviour for the eclipse model.

Ephemerides

In the thesis, the position of the Sun and the Moon are obtained through propagation of the Earth in the Sun-Earth system and the Moon in the Earth-Moon system. Modelling of the positions in this manner lead to errors with respect to the true ephemerides. A comparison is made between the positions used in the thesis simulations and

the values from NASA's SPICE toolkit [28]. The errors in the distance of the Sun and the Moon to the sail are shown as a percentage of the distances obtained from the SPICE toolkit in Table A.2.

**Table A.2:** Error quantification between simulated ephemerides and NASA's SPICE ephemerides

Moment during year	Error position Sun [%]	Moment during month	Error position Moon [%]
Spring equinox	$2.2 \cdot 10^{-2}$	0 weeks	$3.8 \cdot 10^{-1}$
Summer solstice	$2.3 \cdot 10^{-2}$	1 week	$5.1 \cdot 10^{-1}$
Autumn equinox	$2.1 \cdot 10^{-2}$	2 weeks	$2.9 \cdot 10^{-1}$
Winter solstice	$2.3 \cdot 10^{-2}$	3 weeks	$3.4 \cdot 10^{-1}$

As can be seen from Table A.2, the position errors are relatively minor, though larger for the position of the Moon de to nutation, precession and similar effects. However, the differences between simulated positions and positions from ephemerides are small enough that the errors are not a point of concern.

A.1.2. Integration and propagation
RK4 integrator
A comparison between propagator accuracies for a propagation without disturbing accelerations is shown in Figure A.3. Since only terrestrial point mass gravity is used, a circular orbit should stay circular indefinitely. A circular orbit with a semi major axis of $4.2167 \cdot 10^4$ km forms the benchmark solution and propagated orbits after a number of revolutions are compared to this circular orbit. A Runge-Kutta 4 integrator was used with a simulation time of 50000 seconds for both a Cowell propagator and an MEOE propagator. The results are shown in Figure A.3.
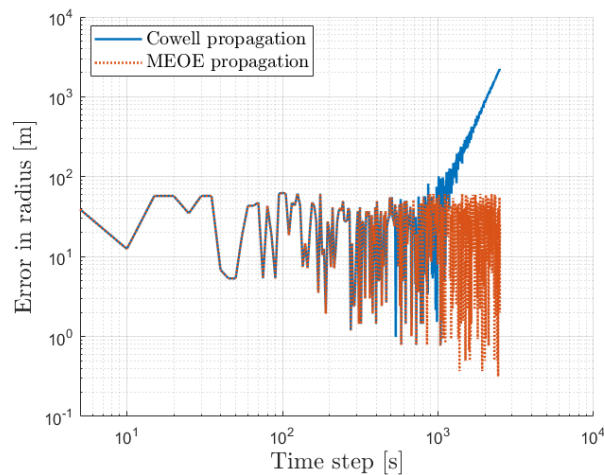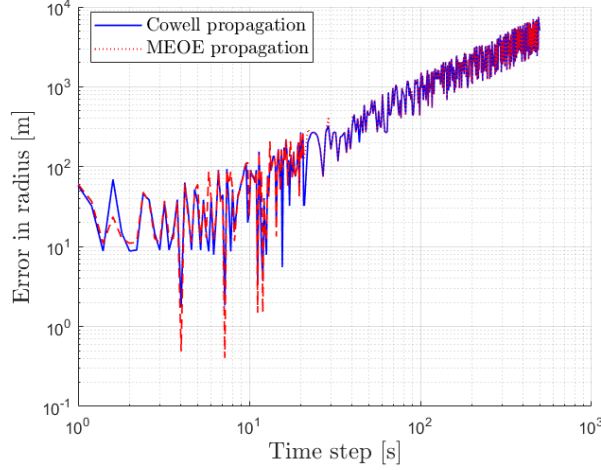

Figure A.3: Comparison between propagation accuracy for different time steps for Cowell propagation and modified equinoctial element propagation for a circular orbit without perturbations.

It can be seen that from time steps of 1000 seconds and above, a linear correlation in the log-log plot between time step and propagation error is present for the Cowell propagator, while for time steps smaller than 1000 seconds the propagation error oscillates in the same order of magnitude. In this constant region, the error is due to rounding errors, while in the linear region the error is mostly due to inherent propagator errors. For the MEOE propagation, there is no inherent propagator error visible.

Propagation
Next, a comparison is performed between the benchmark situation and simulations with different simulation settings and time steps. The complete dynamical model with a longer propagation time is used to assess the error in more practical cases. The propagation time is extended to 500000 seconds. For these simulations, a lightness number of 0.005 is used. Step sizes between 1 and 500 seconds are used, and the results were compared with a simulation with a step size of 0.1, representing the benchmark solution. The results are shown for a Cowell propagator and an MEOE propagator in Figure A.4.

The results from the Cowell propagation and the MEOE propagation closely match with no significant differences, as the region between one and twenty seconds for the time step is dominated by random rounding errors. Figure A.4 nevertheless gives important information about the transition between the region of rounding error and propagator error, which is visible at time steps of approximately thirty seconds. In the context of this thesis and

Figure A.4: Comparison between propagation accuracy for different time steps for Cowell propagation and modified equinoctial element propagation for a representative propagation.

based on additional simulations, a time step of 50 seconds is used.

A.2. Control laws

A.2.1. A^{n}D blending law

Regarding the A^{n}D blending law, few examples from literature are deemed suitable for reproduction for verification purposes, as few test cases include only semi-major axis and eccentricity steering. A related example is found in Macdonald (2005), where a preliminary version of the A^{n}D blending law is used for determining realistic Earth-escape trajectories [16]. In this case, the locally optimal steering law for semi-major axis steering is used in combination with a locally optimal steering law for pericenter change.

The locally optimal steering law for the pericenter is used to prevent close encounters between the sail and the Earth, especially near the end of the Earth-escape trajectory. Blending these control laws occurs like described in the thesis:

$$\vec{\lambda}_b^{\mathcal{E}_{RTN}} = \frac{\sum_k W_k \cdot \vec{\lambda}_k^{\mathcal{E}_{RTN}}}{|\sum_k W_k|} \tag{A.1}$$

As in the thesis, $\vec{\lambda}_b^{\mathcal{E}_{RTN}}$ is the blended steering vector, $\vec{\lambda}_k^{\mathcal{E}_{RTN}}$ is the steering vector for the orbital element k and W_k is the weight function for the orbital element k. The weight functions are defined differently for the case of Earth-escape trajectories compared to the A^{n}D blending method. For this Earth-escape case, the weight functions are a function of the radius of pericenter in the following way:

$$W_f = \frac{r_p}{10^6} - 2.5 \tag{A.2}$$

$$W_a = \exp\left(\frac{W_f}{10}\right) \tag{A.3}$$

$$W_{r_p} = \frac{2500}{\exp\left(W_f\right)} \tag{A.4}$$

$$\tag{A.5}$$

These weight functions are illustrated by Figure A.5 for different values of r_p. The weights are of equal magnitude at an altitude of 10000 km. For smaller altitudes, especially smaller than 7500 or 5000 km, the weight function for the radius of pericenter W_{r_p} is completely dominant. Due to exponential decay of W_{r_p}, the weight function for the semi-major axis steering law W_a is completely dominant for altitudes above 15000 km. This guarantees that the main steering law, which is the one of the semi-major axis, is used whenever possible.

The simulation environment used for verification is focused on Earth-escape trajectories starting from geostationary orbit. A sailcraft has escaped Earth when $e > 1$. An ideal solar-sail model is used by Macdonald and apart from the SRP acceleration and the point-mass gravity of Earth, no additional accelerations are included in
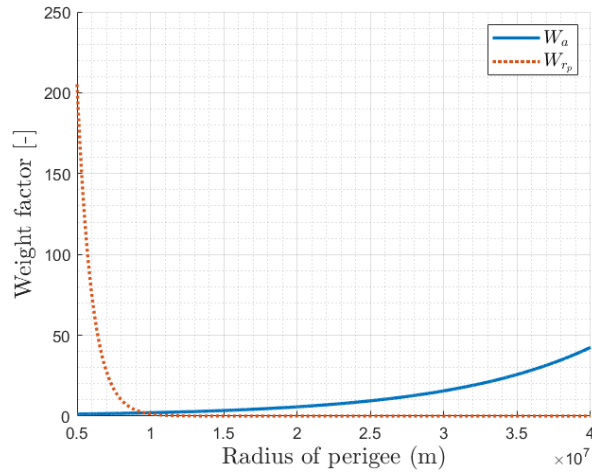
Figure A.5: Weight dependence on the radius of pericenter

the simulation. Propagation is done through MEOEs and a variable step-size DOPRI-78 integrator with absolute and relative tolerances of 10^{-9}.

The simulation environment used in this thesis does not include a DOPRI-78 integrator, and thus a RK4 integrator with a small step size is used, namely 50 seconds. Using smaller step sizes did not make a noticeable difference. The results of the Earth-escape times for a variety of sail areas are shown in Figure A.6.
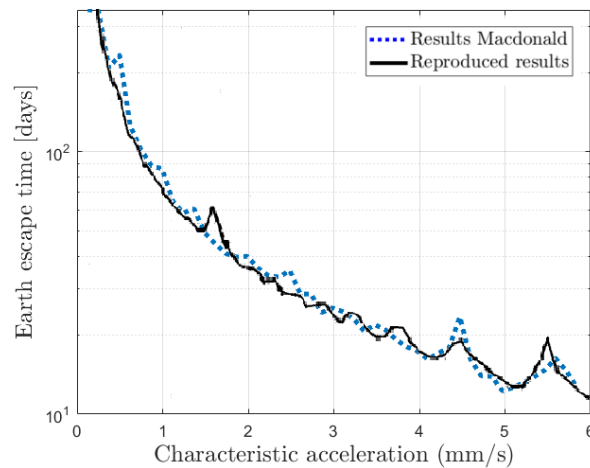
Figure A.6: Reproduced results for the Earth-escape times as a function of characteristic acceleration with overlaid the results as published in Macdonald (2005) [16].

Figure A.6 shows the Earth escape time for different characteristic accelerations, both for the reproduction and for the values from literature. The reproduction is evidently not perfect, but shows the general behaviour of the Earth-escape time as a function of the characteristic acceleration. The peaks, which are due to the fact that the semi-major axis can only be raised during half of the orbit, are generally reproduced well. Only with characteristic accelerations above 5 mm/s, there is a slight discrepancy between reproduced results and the results from literature. This discrepancy is more obvious with larger values of the characteristic acceleration as the simulation times are shorter here and the accelerations in the dynamical model are larger, which causes differences between the simulations to become more obvious.

A.3. Hybrid SEP/SRP thrust

In this section, the shape of the contour for the total acceleration is analysed for small values of $|\vec{a}_{SEP}|$. For this analysis, the value of $\frac{ds_d}{ds_1}$ for each point on both the SRP-acceleration contour and the total acceleration contour is calculated and the difference is taken. The total acceleration contour is described as follows:

$$s_1' = s_1 - \zeta \frac{ds_d}{d\alpha} = s_1 - \zeta(-3\sin{(\alpha)}\cos{(\alpha)}^2) = (3\zeta + 1)(\sin{(\alpha)}\cos{(\alpha)}^2)) \tag{A.6}$$

$$s_d' = s_d + \zeta \frac{ds_1}{d\alpha} = s_d + \zeta(\cos{(\alpha)}^3 - 2\sin{(\alpha)}^2\cos{(\alpha)}) = (\zeta + 1)\cos{(\alpha)}^3 - 2\zeta\sin{(\alpha)}^2\cos{(\alpha)} \tag{A.7}$$

The SRP-acceleration contour can be described by the following formula:

$$s_1 = \sin{(\alpha)} \cdot \cos{(\alpha)}^2 \tag{A.8}$$

$$s_d = \cos{(\alpha)}^3 \tag{A.9}$$

The value $\frac{ds_d}{ds_1}$ is obtained by discretising s_d and s_1 and taking the difference $\frac{s_{d_{i+1}} - s_{d_i}}{s_{1_{i+1}} - s_{1_i}}$ with i ranging from one to the number of discretisation points minus one. The results for the cone angle α ranging from -90 to 90 deg and step sizes of $\frac{\pi}{10^6}$ with the value $|\vec{a}_{SEP}| = \frac{a_c}{2}$ is shown in Figure A.7.
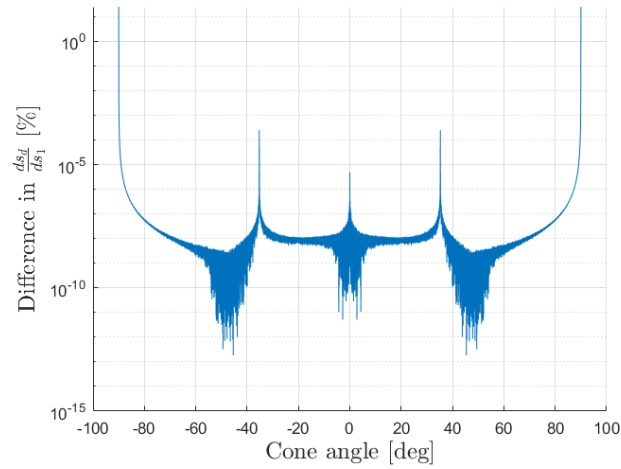
Figure A.7: Relative difference in magnitude of $\frac{ds_d}{ds_1}$ over the SRP-acceleration contour and total acceleration contour.

Most of the graph shows values for the relative difference in the range of 10^{-8} % or smaller, except for $\alpha = -90°$, $\alpha = -35.26°$, $\alpha = 0°$, $\alpha = 35.26°$ and $\alpha = 90°$. For $\alpha = +/-35.26°$, it holds that the value of $\frac{ds_d}{ds_1}$ approaches infinite, while for the other mentioned values for α it holds that the value of $\frac{ds_d}{ds_1}$ approaches zero. From Figure A.7 it can be deduced that for $|\vec{a}_{SEP}| = \frac{a_c}{2}$ and smaller, the total acceleration contour has a very similar shape to the SRP-acceleration contour.